Biochemistry and Chemical Biology
Microbiology and Infectious Disease

The nanoscale organization of the Nipah virus fusion protein informs new membrane fusion mechanisms

Reviewed Preprint
v2 • November 8, 2024
Revised by authors

Reviewed Preprint
v1 • May 1, 2024

Qian Wang, Jinxin Liu, Yuhang Luo, Vicky Kliemke, Giuliana Leonarda Matta, Jingjing Wang, Qian Liu

Institute of Parasitology, Faculty of Agricultural and Environmental Sciences, McGill University, Quebec, Canada • McGill Center for Viral Diseases, Lady Davis Institute, Montreal, Canada

eLife Assessment

This **valuable** study advances our understanding of how Nipah virus fusion protein F (NiV-F) organizes into nanoclusters on cell and viral membranes using biochemical and super-resolution microscopy methods. The conclusions are supported by **solid** evidence and the revision has addressed most of the reviewers' concerns. The relationship between clustering and fusion is of high interest and an interesting hypothesis to continue investigating in future studies.

https://doi.org/10.7554/eLife.97017.2.sa4

Abstract

Paramyxovirus membrane fusion requires an attachment protein for receptor binding and a fusion protein for membrane fusion triggering. Nipah virus (NiV) attachment protein (G) binds to ephrinB2 or -B3 receptors, and fusion protein (F) mediates membrane fusion. NiV-F is a class I fusion protein and is activated by endosomal cleavage. The crystal structure of a soluble GCN4-decorated NiV-F shows a hexamer-of-trimer assembly. Here, we used single-molecule localization microscopy to quantify the NiV-F distribution and organization on cell and virus-like-particle membranes at a nanometer precision. We found that NiV-F on biological membranes forms distinctive clusters that are independent of endosomal cleavage or expression levels. The sequestration of NiV-F into dense clusters favors membrane fusion triggering. The nano-distribution and organization of NiV-F are susceptible to mutations at the hexamer-of-trimer interface, and the putative oligomerization motif on the transmembrane domain. We also show that NiV-F nanoclusters are maintained by NiV-F-AP-2 interactions and the clathrin coat assembly. We propose that the organization of NiV-F into nanoclusters facilitates membrane fusion triggering by a mixed population of NiV-F molecules with varied degrees of cleavage and opportunities for interacting with the NiV-G/receptor complex. These observations provide insights into the in-situ organization and activation mechanisms of the NiV fusion machinery.

Introduction

The family of *Paramyxoviridae* contains many clinically important viruses, such as human parainfluenza virus 1-3, measles virus, and Nipah virus (NiV). Paramyxoviruses code for two glycoproteins on the viral membranes for virus-cell membrane fusion. The receptor-binding proteins (RBP, HN/H/G) engage the host receptors and activate the refolding of the fusion protein (F) that merges the virus and cell membranes[1]. Paramyxovirus-F is a class I fusion protein, along with human immunodeficiency virus (HIV) envelope, influenza virus hemagglutinin, and severe acute respiratory syndrome coronavirus-2 (SARS-CoV-2) spike[1]. Paramyxovirus-F is a trimeric transmembrane protein with a "tree-like" structure at its prefusion conformation. Upon triggering by the RBP/receptor complex, paramyxovirus-F mediates fusion by inserting its N-terminal fusion peptides into the target membrane and undergoes a conformational change from pre- to post-fusion conformations, similarly to other class I fusion proteins. The refolding of the paramyxovirus-F overcomes the energy barrier for membrane fusion and leads to virus-cell and cell-cell membrane fusion.

NiV is a well-studied paramyxovirus due to its capability of human-human and human-animal transmissions, high mortality and morbidity rates, and the unavailability of vaccines or therapeutics for human use[2,3]. NiV is closely related to Hendra virus, Cedar virus, and the newly identified Langya virus[4]. NiV-F is expressed on the cell surface as an fusion-inactive form, activated in the endosome by cathepsin B and L cleavage, and exocytosed to the cell surface as a fusion-active form[5,6]. NiV-G binds to ephrinB2 and/or -B3 receptors in host cells and triggers the refolding of F that leads to virus-cell membrane fusion[7]. Three complementary models of the NiV fusion activation mechanism have been proposed in the past. *In the first model*, the NiV-G and F form a complex before receptor engagement. The F/G interaction maintains F at a prefusion conformation. The receptor binding to G induces conformational changes in G, leading to the release and refolding of F. This model is supported by co-immunoprecipitation and conformational antibody binding assays[8,9]. *In the second model*, NiV-F exists as hexamer-of-trimers, and the fusion peptides are sequestered at the hexameric interface. The activation of one single trimer by the NiV-G/ephrinB2 complex can be transmitted to all six trimers via the interfaces of the hexamer-of-trimers, leading to efficient F-triggering and fusion pore formation. This model is supported by the crystal structure of a GCN4-decorated NiV-F ectodomain and mutagenesis analysis of key amino acid residues at the hexameric interfaces[10]. *In a third model*, NiV-F and G do not form a complex before receptor binding. The NiV-G/ephrinB2 engagement clusters ephrinB2 and triggers F. F triggering leads to reduced mobility of a portion of F molecules that potentially contributes to fusion pore formation. This model is supported by the nanoscale distribution of NiV-F and G on cell membranes resolved by super-resolution microscopy and a single-particle tracking assay of NiV fusion protein at the interface between supported lipid bilayer and live cell membranes[11,12]. Although these models explain the NiV membrane fusion mechanisms from different perspectives, a link between the molecular structure and the fusion machinery on biological membranes remains unclear.

We attempted to address this link by analyzing the nano-organization of NiV-F at the prefusion state on biological membranes using single-molecule localization microscopy (SMLM) and mutagenesis analyses. We have shown that NiV-F forms clusters on biological membranes that are isolated from NiV-G[11]. Here, we show that NiV-F forms regular-sized nanoclusters on cell membranes regardless of the expression level or endosomal cleavage. The estimated size of NiV-F clusters on cell membrane is similar to that of the hexamer-of-trimer assemblies formed by the GCN4-decorated soluble NiV-F. The NiV-F nano-organization is altered by mutations at the hexameric interface and the putative oligomerization motifs at the transmembrane domain. NiV-F molecules enriched in nanoclusters favor membrane fusion activation. The NiV-F nanoclusters are

stabilized by the interactions between NiV-F, the endocytosis adaptor complex AP-2, and the clathrin coat at the cell membranes. In summary, our study reveals the NiV-F nano-organization on the biological membranes and provides novel insights into the NiV fusion machinery *in situ*.

NiV-F forms regular-sized clusters that are not affected by the surface expression level

We recently published that NiV-F formed distinctive nanoclusters on the plasma membrane regardless of the presence of NiV-G or ephrinB2[11]. To investigate the determinants of the NiV-F nano-organization, we used SMLM to probe the NiV-F at various conditions. SMLM generates super-resolution images by localizing spatially far-apart fluorophores with nanometer precision[13]. PK13 cells have a flat morphology that is suitable for SMLM imaging. PK13 cells express little endogenous ephrinB2 and -B3 receptors for NiV and thus can eliminate any potential receptor-dependent clustering. Cell surface NiV-F was detected using a FLAG tag in its extracellular domain[11]. The FLAG tags were employed to detect NiV-F because of the availability of high affinity and specificity anti-FLAG antibodies for a high labeling density, which is vital for the reconstruction accuracy of SMLM images[14]. To rule out the effect of the FLAG tag on NiV-F clustering, we compared NiV-F clusters formed by NiV-F-FLAG to that of a NiV-F-HA construct. Both HA and FLAG tags were inserted after amino acid residue 104, right before the fusion peptide (Fig. S1A). Visual examination of the SMLM images reveals that NiV-F-FLAG and NiV-F-HA form similar clusters (Fig. S1B). The clustering tendency, indicated by Hopkins' index, is comparable between NiV-F-HA and NiV-F-FLAG (Fig. S1C), suggesting that NiV-F clustering is not affected by specific epitope tags. To test whether the FLAG tag affects the function of NiV-F, we pseudotyped NiV-G-HA and NiV-F-FLAG or un-tagged NiV-F on the recombinant vesicular stomatitis virus (VSV) with glycoprotein (G) replaced by a *Renilla* luciferase gene (VSV-ΔG-rluc) and determined the viral entry levels (VSV/NiV pseudoviruses). The virus entry induced by NiV-F-FLAG is comparable to that of untagged NiV-F (Fig. S1D), verifying that the FLAG tag has minimal effect on the membrane fusion activity of NiV-F.

Next, we investigated whether the nano-organization of NiV-F depends on the cell surface expression levels. The total cell surface expression level (CSE) of NiV-F in a selected cell was measured before the cell was subjected to SMLM imaging. The SMLM images show that NiV-F forms similar nanoclusters in both high-expression and low-expression cells (**Fig. 1A and B**).

Our data show that the clustering tendency of NiV-F is independent of its CSE in individual cells (**Fig. 1C**). To gain a quantitative understanding of NiV-F nanoscale organization, we used a cluster identification method DBSCAN (Density-Based Spatial Clustering of Applications with Noise) that links the closely situated localizations in a propagative manner. We created cluster and density maps using Clus-DoC for representative high-expression and low-expression cells (**Fig. 1D and E**)[15]. Our data show that the estimated diameter of the NiV-F clusters ranges from 20-34 nm, with a peak at 24 nm (**Fig. 1F**). Nonetheless, the precise values of the cluster diameter are indicative rather than definite in SMLM as it could be affected by the labeling complex and the blinking property of the fluorophore. The distribution of the cluster diameter shows that ~60% of NiV-F clusters have similar sizes, indicating that NiV-F clusters maintain a quite uniform appearance. Interestingly, we noticed that the size of the clusters (**Fig. 1G**) and localization density (**Fig. 1H**) in clusters were similar between high- and low-expression cells, suggesting that the NiV-F organization in nanoclusters is not affected by the expression levels. Moreover, our data show that the high-expression cells have more clusters than the low-expression cells (**Fig. 1I**). These results suggest that changes in CSE may affect the number of NiV-F clusters on the plasma membrane (**Fig. 1I**), but not the clustering tendency of NiV-F (**Fig. 1C**), the size of the clusters (**Fig. 1G**), or the localization density within clusters (**Fig. 1H**). These data imply that the distribution and nano-organization of NiV-F are tightly regulated and may be important for membrane fusion activation. We also analyzed NiV-F distribution in different cell lines. HeLa cells express ephrinB2 and -B3, and thus are NiV permissive cells. The overall NiV-F nano-organization

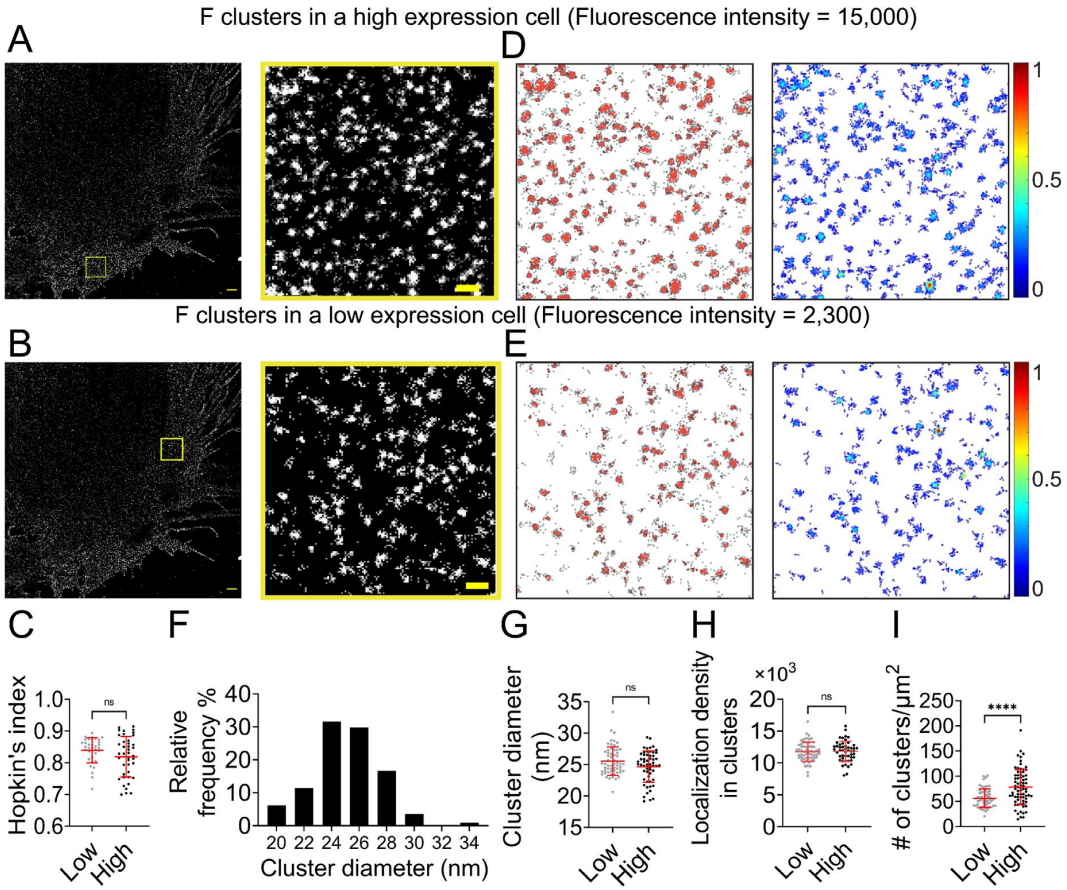

Fig. 1.

NiV-F forms regular-sized clusters that are not affected by the surface expression level.

(A and B) Cross-section (Δz = 600 nm) of SMLM images of NiV-F in high-expression (A) and low-expression (B) PK13 cells. Scale bar: 1 μm. The yellow boxed region is enlarged to show the detailed distribution pattern. Scale bar: 0.2 μm. (C) Hopkin's index of the F localizations in low- and high-expression cells. n = 35 and 40. (D and E) Cluster maps (left) and localization density maps (right) of the enlarged regions in A and B. Cluster contours are highlighted with gray lines. Normalized relative density is pseudocolored according to the scale on the right. (F) The percentage distribution of the NiV-F cluster diameter from 13 cells. n = 133. (G) The cluster diameters in low- and high-expression cells. n = 58 and 56. (H) The localization density (# of localizations per μm^2) within clusters in low- and high-expression cells. n = 58 and 50. (I) The number of clusters per μm^2 in low- and high-expression cells. n = 59 and 74. The cut-off fluorescence intensity for low- and high-expression cells is 8000 (Arb. Unit). Sample size n is the number of total regions from 6-8 cells. Bars represent mean ± SD. P value was obtained using the Mann-Whitney test. ns: $p > 0.05$; * $p<0.01$; ** $p<0.001$; *** $p<0.0001$.

seems quite similar on PK13 and HeLa cells, agreeing with our previous results (Fig. S2A)[11]. The Hopkins' indices are also similar for NiV-F on PK13 and HeLa cells (Fig. S2B). The DBSCAN analysis shows that the percentage localizations in clusters (Fig. S2C), the relative density defined as the ratio of the localization density in clusters to the total localization density in the selected region (Fig. S2D), and cluster diameters (Fig. S2E) are comparable for NiV-F on PK13 and HeLa cells. These results suggest that NiV-F clusters are minimally affected by the cell lines of expression or the presence of the ephrinB2 and/or -B3.

The NiV-F nanoclusters are not affected by NiV-F cleavage

NiV-F is synthesized in host cells as inactive precursor F_0 and cleaved by cellular proteases cathepsin L and cathepsin B in the endosomes at an acidic pH to generate the fusion-active, disulfide-linked F_1-F_2 construct. The F_1-F_2 is subsequently recycled to the cell surface to induce cell-cell fusion and incorporated into virus particles. We hypothesized that the F_0 precursor and the F_1-F_2 active forms co-existed in the same clusters on the cell surface. To test this hypothesis, we used a pan-cysteine cathepsin inhibitor E64d to inhibit the NiV-F cleavage. E64d inhibited the cell-cell fusion induced by NiV-F and NiV-G in HeLa cells (Fig. S3), agreeing with the previous fusion inhibitory effects in Vero and MDCK cells[5,6]. Our SMLM images show that E64d treatment does not result in any significant change in the clustering of NiV-F in HeLa cells (**Fig. 2A**). The clustering extent of NiV-F was not altered by the E64d treatment, as shown by comparable Hopkin's indices (**Fig. 2B**). Additionally, quantitative parameters of the nano-organization such as percentage of localizations in clusters (**Fig. 2C**), relative density (**Fig. 2D**), cluster size (**Fig. 2E**), and the total density of the regions (**Fig. 2F**) were comparable. Our data show that clusters formed by non-cleaved NiV-F in cells treated by E64d are similar to those formed by a mixture of cleaved and non-cleaved NiV-F in the control cells, suggesting that F cleavage does not alter F clustering on the cell membrane. These data support our hypothesis that the non-cleaved precursor F_0 and cleaved F_1-F_2 coexist in the same cluster on the cell membrane.

Mutations destabilizing the NiV-F hexamer-of-trimer assembly alter its nano-organization on the plasma membrane

We noticed that the uniformity in the NiV-F cluster morphology resembled the hexameric assembly of soluble NiV-F decorated by GCN4[10]. Next, we investigated whether NiV-F clusters were stabilized by the hexameric interface. As reported, L53D and V108D mutants destabilize the hexameric interface and demonstrate decreased membrane fusion ability; Q393L stabilizes the hexameric interface and demonstrates increased fusion ability[10]. We inserted the FLAG tag into the ectodomains of these mutants at the same position as that of the NiV-F. We verified that the relative fusion ability to their F-WT counterpart was comparable between the FLAG-tagged and untagged mutants (Fig. S4A and S4B)[10]. The FLAG-tagged mutants showed similar CSE levels to NiV-F (Fig. S4C). All mutants showed some levels of processing, although the cleavage of L53D was the least efficient compared to F-WT and other mutants (Fig. S4D).

Additionally, the FLAG-tagged NiV-F mutants showed a similar trend in virus entry as that of cell-cell fusion when pseudotyped to a recombinant VSV virus (Fig. S4E and S4F), agreeing with the previous results obtained using the NiV-F constructs with a C-terminal AU1 tag[10]. We also generated VLPs expressing NiV-M-β-lactamase (NiV-M-Bla), NiV-G-HA, and NiV-F-FLAG or mutants for an entry kinetics assay. The entry kinetics was measured in real-time by conversion of green to blue fluorescence resulting from CCF2-AM dye cleavage by the β-lactamase upon the entry of VLPs[16,17]. Our results show that the hyperfusogenic mutant Q393L shows more efficient VLP entry than that of WT, while VLPs bearing the hypofusogenic mutant L53D and V108D are less efficient in entry than that of the WT (Fig. S4G and S4H). It is noteworthy that the incorporation of NiV-G seems to be impacted by the expression of L53D in both VSV/NiV pseudovirions and VLPs (Fig. S4F and S4H), and the deficient virus entry induced by L53D may be partly due to the decreased attachment to the target cells (Fig. S4E and S4G). Nonetheless, the level of L53D on the

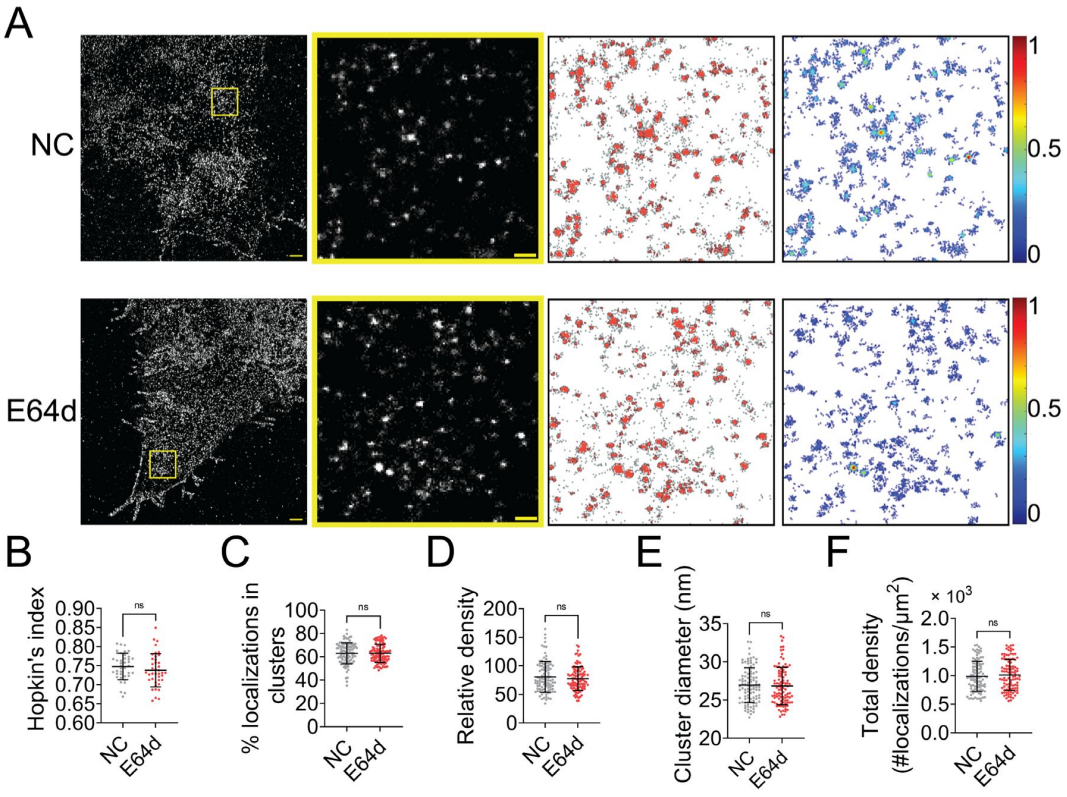

Fig 2.

Endosomal cleavage does not affect the nanoscale distribution of NiV-F.

(A) First column: Cross-section (Δz = 600 nm) of SMLM images of NiV-F in HeLa cells untreated (NC) and treated with 20 μM E64d (E64d). HeLa cells were co-transfected by expression plasmids coding for NiV-G and NiV-F. Twenty μM E64d or the same volume of solvent methanol was added to cells at 2 hrs post-transfection. Scale bar: 1 μm. Second column: The yellow boxed region in the first column is enlarged to show individual clusters. Scale bar: 0.2 μm. Third column: Cluster maps from the enlarged regions. Fourth column: Localization density maps show the normalized relative density of the enlarged regions. (B-F) Quantitative analyses of NiV-F clusters formed in HeLa cells without (NC) and with (E64d) the E64d treatment: (B) Hopkin's index, n = 40 and 40; (C) percentage of localizations in clusters, n = 101 and 101; (D) relative density, n = 100 and 103; (E) average cluster diameters, n = 100 and 101; (F) total density of the region, n = 101 and 102. Bars represent mean ± SD. p value was obtained using Mann-Whitney test. ns: $p > 0.05$; * $p<0.01$; ** $p<0.001$; *** $p<0.0001$. Sample size n is the number of total regions from 4-10 cells.

pseudovirions and VLPs seems comparable to that of the WT (Fig. S4F and S4H). These data support that mutations at the hexameric interface significantly impact the fusion activity of NiV-F on both cell and virus surface.

NiV-F mutants L53D, V108D, and Q393L were expressed on PK13 cells and subjected to SMLM imaging. The images show that clusters formed by L53D and V108D are smaller and more dispersed than those of the F-WT and Q393L (**Fig. 3A**). The Hopkin's index for Q393L is significantly higher than that of F-WT, while the Hopkin's indices for L53D and V108D are slightly lower than that of F-WT (**Fig. 3B**). Consistently, a lower percentage of L53D and V108D localizations are segregated into clusters than that of F-WT, while a similar percentage of Q393L and F-WT localizations form clusters (**Fig. 3C**). In addition, clusters of L53D and V108D are less packed than that of F-WT, with 48-, 49-, and 55-fold denser than the total localization density in the region, respectively (**Fig. 3D**). The clusters of Q393L are not significantly denser than that of F-WT (**Fig. 3D**). Our analysis also shows that L53D and V108D form smaller clusters compared to the F-WT (**Fig. 3E**). The Q393L clusters are of a similar size to that of F-WT (**Fig. 3E**). The total density of localizations and the total CSE levels for all constructs are comparable (**Fig. 3F** and Fig. S4C), suggesting that differences in clustering are not due to variable numbers of localizations or levels of expression. Collectively, these data show that the mutations destabilizing the hexameric interface (L53D and V108D) make NiV-F localizations more dispersed and form smaller and less packed clusters. Q393L that stabilizes the hexameric interface promotes the clustering of NiV-F localizations (**Fig. 3B**) but does not significantly alter the organization and morphology of individual clusters (**Fig. 3C-F**). These data suggest that the NiV-F clusters are susceptible to mutations at the hexameric interface. Considering that the uniformed cluster size is similar to the assemblies formed by the soluble GCN4-NiV-F, we propose that NiV-F may organize into hexamer-of-trimer on the plasma membrane.

Mutations at the NiV-F hexameric interface affect its distribution on the VLP membrane

To further investigate the organization of F mutants in viral membranes, we imaged the FLAG-tagged NiV-F constructs on VLPs produced by 293T cells expressing NiV-M-GFP, NiV-G, and NiV-F-WT, L53D, V108D, or Q393L mutants. The incorporation of NiV-F is comparable among the NiV-F constructs (**Fig. 4A**). The L53D and V108D on VLPs are less cleaved compared to that of the F-WT and Q393L, as suggested by the weaker NiV-F_2 bands (**Fig. 4A**). Notably, the incorporation of NiV-G is largely abrogated in the VLPs that expressing L53D (**Fig. 4A**).

To probe the organization of NiV-F constructs on VLPs, the F-constructs on VLP membranes were stained using Alexa Fluor 647 and subjected to SMLM imaging. The GFP fluorescence on NiV-M was used to locate the VLPs. **Fig. 4B** shows that F-WT and F-Q393L form distinctive clusters, while localizations of L53D and V108D are more dispersed on a z = 100 nm projection. This agrees with their distributions on the plasma membrane (**Fig. 3A**). To gain a quantitative insight into the distribution of the F constructs on the three-dimensional (3D) VLPs, we used an algorithm named OPTICS (Ordering Points To Identify Clustering Structure)[18]. To identify clusters, the OPTICS algorithm sorts out the localizations by calculating the reachability distance between two adjacent localizations in a propagative manner and generates a sequence of the ordered localizations[18]. In the plot of reachability distance vs. the sequence of ordered localizations, a sudden increase in the reachability distance marks the cutoff of a cluster (Fig. S5A). The shade between neighboring peaks represents localizations that are classified in one cluster (Fig. S5A). OPTICS can identify sub-clusters on a 3D VLP that may not be recognized by DBSCAN that uses one fixed parameter for the entire dataset. Fig. S5B shows the OPTICS plots of the localizations of F-WT and mutants on representative VLPs (**Fig. 4B**).

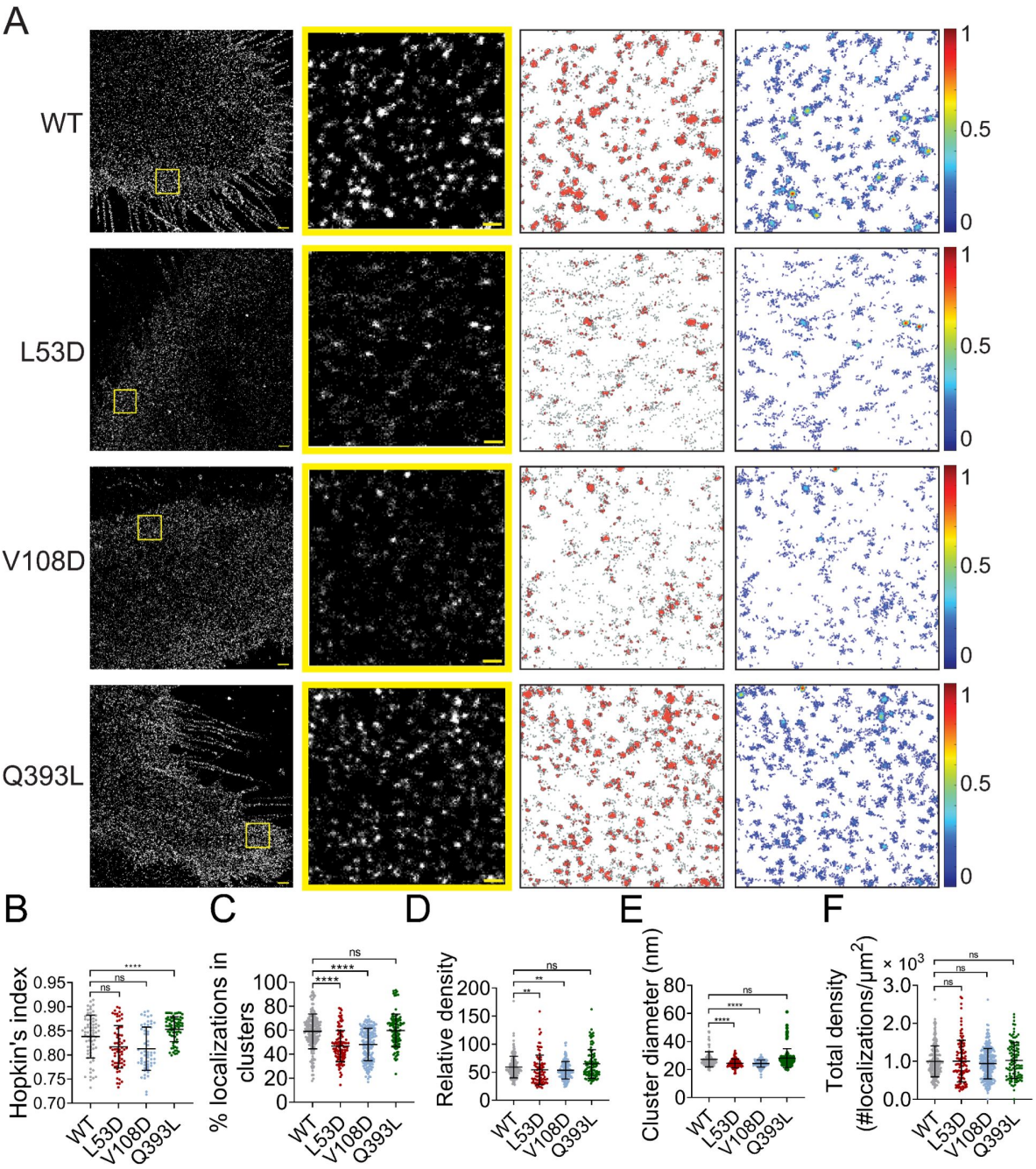

Fig. 3.

Mutations at the NiV-F hexameric interface affect its nano-organization.

(A) First column: Cross-section (Δz = 600 nm) of SMLM images of the FLAG-tagged NiV-F-WT (WT), L53D, V108D, and Q393L on PK13 cell membrane. Scale bar: 1 μm. Second column: The yellow boxed regions in the first column are enlarged to show individual clusters. Scale bar: 0.2 μm. Third column: Cluster maps from enlarged regions. Fourth column: Localization density maps show normalized relative density of the enlarged regions. (B-F) Quantitative analyses of the distribution of the FLAG-tagged NiV-F constructs: (B) Hopkin's index, n = 57-70; (C) Percentage of localizations in clusters, n = 106-198; (D) Relative density, n = 90-187; (E) Average cluster diameters, n = 106-196; (F) total density of the region (a ratio of total localizations in a region to the size of the region), n = 105-242. Bars represent mean ± SD. Sample size n is the number of total regions from 11-20 cells. p value was obtained using Mann-Whitney test. ns: $p > 0.05$; * $p<0.01$; ** $p<0.001$; *** $p<0.0001$.

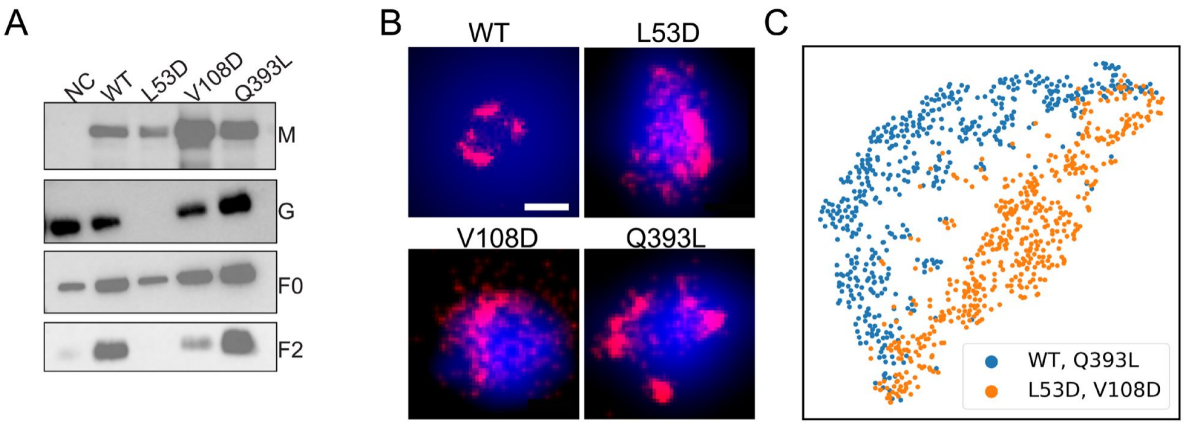

Fig. 4.

The distribution and organization of NiV-F constructs in VLPs.

(A). The incorporation of F-WT and mutants in VLPs. NiV-M-GFP, G-HA, and FLAG-tagged F-WT or mutants were transfected to 293T cells. The supernatants were collected at 48 hrs post-transfection and analyzed on SDS-PAGE followed by western blotting. NiV-M was probed by polyclonal goat anti-GFP, NiV-G polyclonal rabbit anti-HA, F_0 and F_2 M2 monoclonal mouse anti-FLAG antibody. (B) Cross-section (Δz = 100 nm) of SMLM images of the FLAG-tagged NiV-F-WT (WT), L53D, V108D, and Q393L on individual VLPs. Scale bar: 0.2 μm. (C) The classification of the ordered sequence of reachability distances of the NiV-F constructs localizations. Orange: F-WT (n = 306) and Q393L (n = 323); Blue: L53D (n = 310) and V108D (n = 329). n is the number of VLPs used for classification analysis.

The noticeable kinks suggest that F-WT and Q393L form distinctive clusters on VLPs, while the irregular, small kinks indicate that L53D and V108D are more dispersed and form smaller clusters on VLPs (**Fig. 4B** and Fig. S5B). To gain a population insight on the nano-organization of the F constructs on VLPs, we developed a one-dimensional convolutional neural network (1D CNN) to classify the ordered sequence of reachability distances of the NiV-F localizations obtained by the OPTICS algorithm[19]. The distribution patterns of the localizations of the F-WT and Q393L partition into one category, and L53D and V108D in another (**Fig. 4C**). These results indicate that L53D and V108D form smaller and more dispersed clusters than F-WT and Q393L on the VLP membranes, agreeing with that of the plasma membrane (**Fig. 3**). Our results indicate that the trimer-trimer interaction at the hexameric interface is key in stabilizing the nano-organization of NiV-F on both cell and viral membranes, and NiV-F do not seem to rearrange during the incorporation into VLPs. Nonetheless, our data do not rule out the possibility that the association of nucleocapsids with the plasma membrane during assembly may reorganize NiV-F on the authentic virus membranes. Since the incorporation levels of NiV-M and -G varies among mutants, the nano-organization of NiV-F is likely associated with the virion incorporation or budding.

The NiV-F clusters are dispersed upon the disruption of the interactions between transmembrane domains (TMD)

Evidence shows that TMD of class I fusion protein can self-associate in the absence of the rest of the protein and is important for membrane fusion[20]. Previous studies show that mutations in the Leucine-Isoleucine Zipper (LI zipper) motif lead to the dissociation of an HeV-F TMD-derived peptide, decreased stability, and the fusion ability of the whole HeV-F protein[21]. As the TMD domains of the NiV- and HeV-F demonstrate a 94% similarity, we mutated leucine (488 and 509) and isoleucine (495 and 502) residues of the LI zipper in NiV-F TMD to alanine (LI4A) (Fig. S6A). Similar to their counterparts of HeV-F, the NiV-F-LI4A showed a decreased F processing (Fig. S6B), cell-cell fusion activity (Fig. S6C and S6D), and CSE levels (Fig. S6E)[21]. The NiV-F-LI4A failed to incorporate into VSV/NiV pseudovirions (Fig. S6F), and thus did not induce any virus entry (Fig. S6G). Visual inspection of the images suggests that LI4A forms bigger clusters than F-WT (**Fig. 5A**). However, the LI4A seems less likely to cluster than F-WT, indicated by a lower Hopkin's index (**Fig. 5B**). Similarly, the portion of LI4A localizations partitioned into clusters is slightly lower than that of WT (**Fig. 5C**). Interestingly, we noticed that clusters formed by LI4A are significantly bigger (**Fig. 5D**) than that of F-WT and with a similar localization density within the clusters (**Fig. 5E**). The data suggest that interactions between TMDs of NiV-F monomers play a role in stabilizing its nano-organization. Dissociation of TMDs by mutations may result in increased space between F monomers and thus leads to bigger clusters on the cell membrane.

The NiV-F nanoclusters are stabilized by endocytosis components

NiV-F can be endocytosed for endosomal cleavage. Next, we investigated whether NiV-F clusters are stabilized during endocytosis. NiV-F contains an endocytosis sorting signal YSRL and an additional YY motif at its cytoplasmic tail (Fig. S7A). Mutation of these tyrosine residues to alanine almost diminished NiV-F cleavage[6]. A FLAG-tagged NiV-F-YA construct containing the aforementioned mutations resulted in significantly less F_2 band than F-WT (Fig. S7B) and completely abrogated cell-cell fusion in 293T cells (Fig. S7C and S7D), although the CSE levels were comparable to that of F-WT (Fig. S7E). The YA mutant did not incorporate into the VSV/NiV pseudovirions (Fig. S7F) and thus did not mediate virus entry (Fig. S7G). By visually inspecting the SMLM images, we noticed that F-YA was less clustered than that of F-WT (**Fig. 6A**). Indeed, the Hopkin's analysis suggests that F-YA is less clustered than F-WT (**Fig. 6B**). The DBSCAN analysis shows that lower percentage of F-YA localizations segregate into clusters (**Fig. 6C**) than that of the F-WT, and clusters formed by F-YA are smaller (**Fig. 6D**) and less dense (**Fig. 6E**) than that of the F-WT. Notably, there is no significant difference in the total density for F-YA and F-WT SMLM images (**Fig. 6F**), indicating that the differences in cluster organizations do not result from overall protein expression or the stochastic blinking properties of the fluorophore. These results

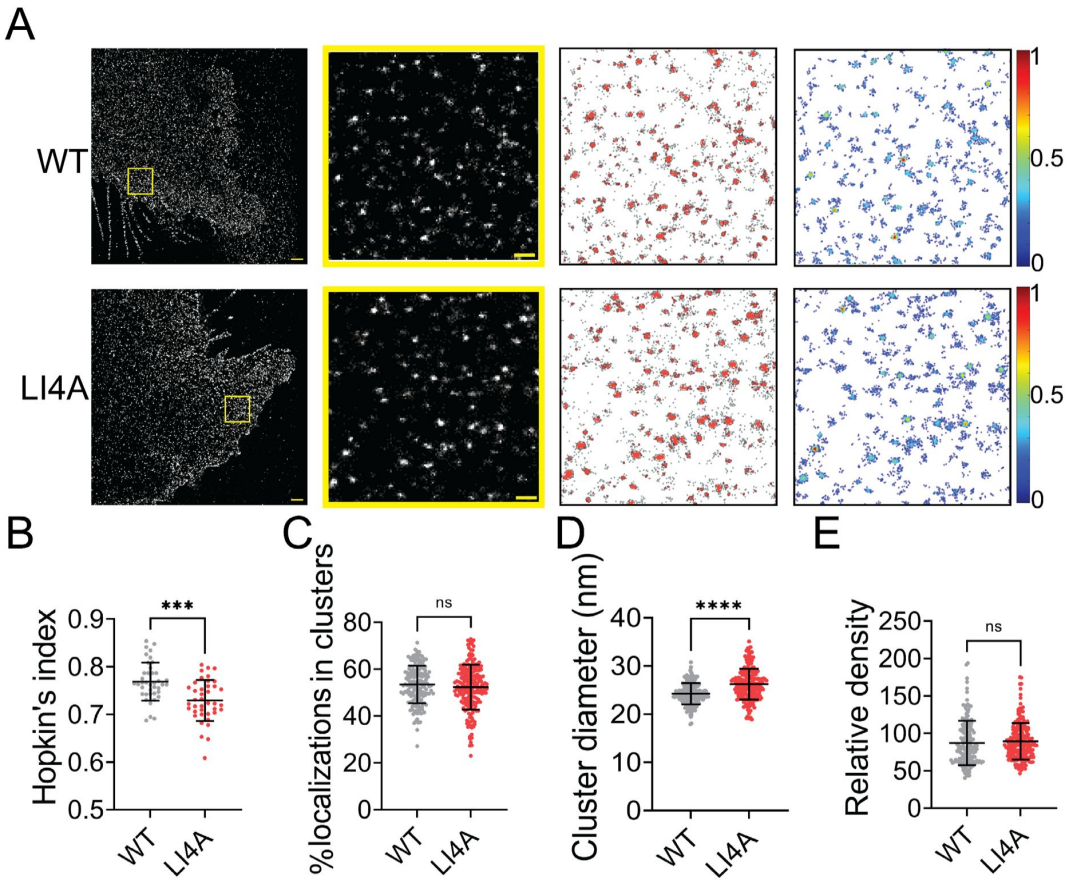

Fig. 5.

Mutations in the LI zipper of the NiV-F transmembrane domain disturbs the NiV-F distribution.

A) First column: Cross-section (Δz = 600 nm) of SMLM images of the FLAG-tagged NiV-F-WT (WT) and NiV-F-LI4A (LI4A) mutant on PK13 cell membrane. Scale bar: 1 μm. Second column: The yellow boxed region in the first column is enlarged to show individual clusters. Scale bar: 0.2 μm. Third column: Cluster maps from enlarged regions. Fourth column: Localization density maps show normalized relative density of the enlarged regions in the second column. (B-E) Quantitative analyses of the WT and LI4A clusters: (B) Hopkin's index, n=40 and 40 (C) Percentage of localizations in clusters, n = 171 and 211; (D) Average cluster diameters, n = 171 and 211; (E) Relative density, n = 166 and 211. Bars represent mean ± SD. p value was obtained using Mann-Whitney test. ns: $p > 0.05$; * $p<0.01$; ** $p<0.001$; *** $p<0.0001$. Sample size n is the number of total regions from 13-16 cells.

suggest that the endocytosis sorting signal of NiV-F may facilitate the enrichment of NiV-F into clusters on the cell surface, preparing them for endosomal cleavage and/or incorporation into viruses.

It is established that the YxxΦ sorting signal on the endocytosis cargo is bound and enriched by the heterotetrameric adaptor protein (AP) complexes, which further recruit the assembly of the clathrin coat[22,23]. We hypothesize that the clustering of NiV-F is promoted by the assembly of the clathrin coat via the NiV-F-AP-2 interactions. As suggested by a yeast two-hybrid analysis, NiV-F interacts with μ1, μ2, μ3 and μ4 subunits of the AP complexes AP-1, AP-2, AP-3, and AP-4, and mutations of Y525, Y542, and Y543 almost completely abolished the interaction between AP-2 and NiV-F[24]. Indeed, the co-immunoprecipitation assay shows that less AP2μ2 is pulled down by F-YA than that of F-WT, suggesting that F-YA has a reduced interaction with AP-2 (Fig. S7H). Next, we examined the NiV-F clusters in HeLa cells treated by the endocytosis inhibitor pitstop2. Pitstop2 blocks clathrin-mediated endocytosis by obstructing the binding of the accessory protein (*e.g.* AP-2) and the clathrin terminal domain, and potentially preventing the assembly of the clathrin coat[25]. The SMLM images (**Fig. 6G**) show that the NiV-F localizations are more dispersed upon pitstop2 treatment, agreeing with the lower Hopkin's index (**Fig. 6H**) and a smaller percentage of localizations in clusters (**Fig. 6I**) in pitstop2 treated group compared to that of the control group. Interestingly, we noticed that the NiV-F clusters in pitstop2 treated cells were larger than the control cells (**Fig. 6J**), although with similar densities (**Fig. 6K**). The total density is consistent between the pitstop2 treated and control groups (**Fig. 6L**). The overall dispersed NiV-F distribution upon pitstop2 treatment may potentially be caused by the disrupted assembly of clathrin coat. In combination, these results suggest that the enrichment of NiV-F by AP-2 and the subsequent assembly of the clathrin-coated endosomes are important in stabilizing the F clusters on cell membranes. We envision that the endocytosis components may also facilitate the NiV-F clustering in virus particles as previous proteomic studies show the presence of endocytosis related proteins, such as clathrin, AP-2, and dynamin in NiV VLPs[26–28].

Discussion

Here we used SMLM to resolve the arrangement and organization of NiV-F on the biological membranes at a precision of 10 nm. Our data supports the following conclusions: 1) NiV-F is organized into nanoclusters on the biological membranes and this organization is independent of the protein expression level or endosomal cleavage; 2) the NiV-F nano-organization is susceptible to mutations at the trimer interface on the NiV-F ectodomain and the putative oligomerization motif on the transmembrane domain; 3) NiV-F sequestered in nanoclusters favors membrane fusion activation; 4) the interactions among NiV-F, the AP-2 complex, and the clathrin coat assembly stabilize the NiV-F clusters. We propose that the NiV-F nanoclusters are the fundamental unit of the NiV fusion machinery, and this organization facilitates membrane fusion triggering by a mixed population of NiV-F molecules with varied degrees of cleavage and opportunities of interacting with NiV-G/receptor complex.

The nano-organization of NiV-F informs the coordinated membrane fusion triggering by a mixed population of NiV-F. This notion is supported by the following observations from this and previous studies: 1) NiV-F molecules form distinctive, regular-sized nanoclusters on the cell and virus membranes (**Fig. 1A-E**); 2) the cleaved, active F co-exist with the noncleaved, inactive F in a nanocluster, as suggested by that the NiV-F nanoclusters are resistant to the cathepsin inhibitor, E64d (**Fig. 2**); 3) the NiV-F and G are segregated into different clusters[11]; and 4) the full-length NiV-F and -G proteins do not show stable interactions either before or after ephrinB2 activation[12]. These observations indicate that the NiV-F triggering may be a result of transient interactions between the F molecules at the edge of the clusters with the adjacent ephrinB2/G complex. Moreover, we observed that the NiV-F sequestering into clusters is favorable for membrane fusion activation (**Fig. 3**, **4**, and 5), highlighting the importance of the spatial

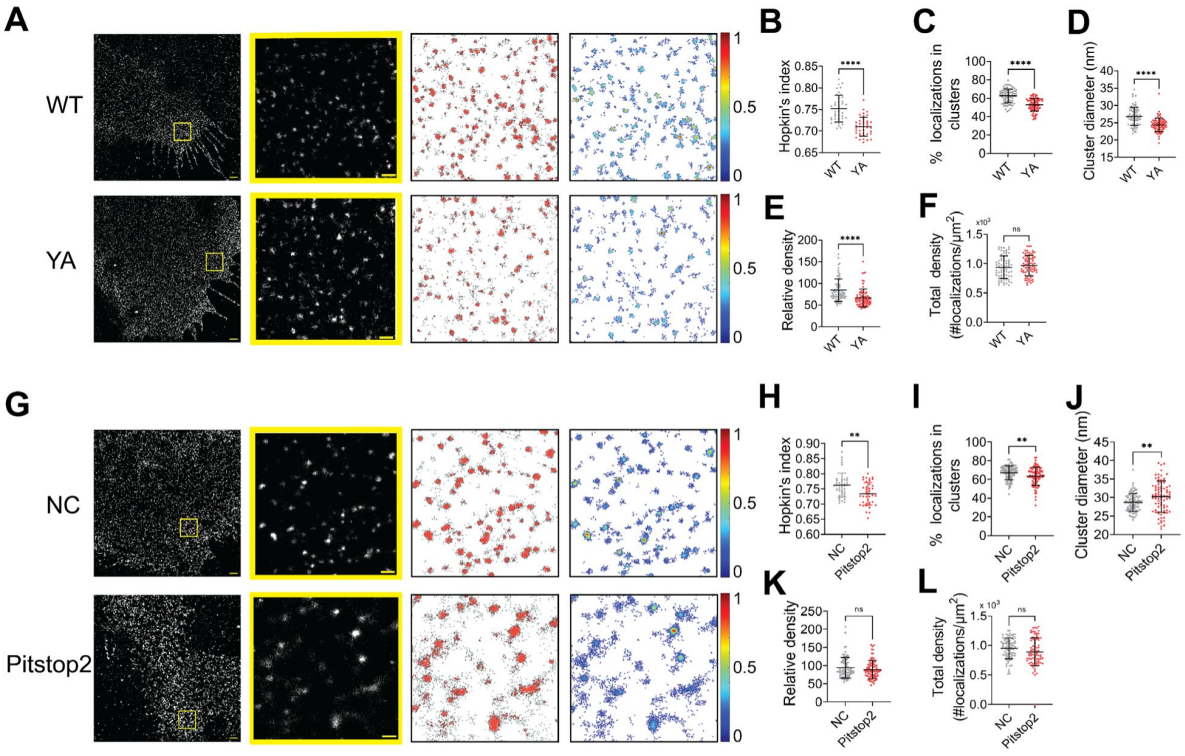

Fig. 6.

The NiV-F nanoclusters are stabilized by endocytosis components.

(A) First column: Cross-section (Δz = 600 nm) of SMLM images of the FLAG-tagged NiV-F-WT (WT) and NiV-F-YA (YA) mutant on PK13 cell membrane. Scale bar: 1 μm. Second column: The yellow boxed region in the first column is enlarged to show individual clusters. Scale bar: 0.2 μm. Third column: Cluster maps from enlarged regions. Fourth column: Localization density maps show normalized relative density of the enlarged regions in the second column. (B-F) Quantitative analyses of the WT and YA clusters: (B) Hopkins index of WT and YA, n = 40 and n = 40; (C) Percentage of localizations in clusters, n = 72 and 77; (D) Average cluster diameters, n = 72 and 77; (E) Relative density, n = 71 and 76; (F) total density of the region, n = 72 and 77. (G) First column: Cross-section (Δz = 600 nm) of SMLM images of the FLAG-tagged NiV-F-WT treated without (NC) and with pitstop2 (pitstop2) on HeLa cell membrane. Scale bar: 1 μm. Second column: The yellow boxed region in the first column is enlarged to show individual clusters. Scale bar: 0.2 μm. Third column: Cluster maps from enlarged regions. Fourth column: Localization density maps show normalized relative density of the enlarged regions in the second column. (H-L) Quantitative analyses of NiV-F without (NC) and with pitstop2 (pitstop2): (H) Hopkins index, n = 40 and n = 40; (I) Percentage of localizations in clusters, n = 82 and 85; (J) Average cluster diameters, n = 82 and 81; (K) Relative density, n = 82 and 81; (L) total density of the region, n = 82 and 81. Bars represent mean ± SD. p value was obtained using Mann-Whitney test. ns: $p > 0.05$; * $p<0.01$; ** $p<0.001$; *** $p<0.0001$. Sample size n is the number of total regions from 4-9 cells.

arrangement of NiV-F in its fusion activity. Therefore, it is likely that the triggered, fusion-active NiV-F at the cluster peripheral can facilitate other F molecules in the same cluster to fulfill the conformational changes, and thus maximize the energy to merge the opposing membranes. In contrast, the correlation between the clustering pattern of NiV-F and its incorporation into virions is not obvious. Although the YA and LI4A mutants that showed aberrant clusters cannot incorporate into VSV/NiV pseudovirions (Fig. S6F and S7F), the clustering-deficient hexameric interface mutants L53D and V108D were incorporated into VLPs (**Fig. 4A**) and VSV/NiV pseudovirisons (Fig. S4F) comparable to that of NiV-F-WT. Therefore, the significance of NiV-F clustering for assembly and budding of the virions may be context-dependent.

A previous study revealed a hexamer-of-trimer assembly of soluble, GCN4-decorated, prefusion NiV-F. Using SMLM, we estimated that the NiV-F clusters on the cell plasma membrane had a diameter between 24-26 nm (**Fig. 1F**). This estimation agrees with the size of the hexameric soluble NiV-F-GCN4 assemblies[10]. Notably, the density of clusters (**Fig. 1I**), but not the size and localization density of individual clusters (**Fig. 1G and H**), is affected by the surface expression levels of NiV-F, implying that the NiV-F clusters are highly regulated. A collaborative effort of multiple copies of viral envelope proteins is favorable for receptor binding and overcoming the energy barrier for membrane fusion. Nanoclusters formed by viral glycoproteins have been observed for HIV-1[29,30], Herpes virus[31], and Influenza virus[32]. The viral restriction factor, serine incorporator protein 5 (SERINC5), inhibits HIV-1 fusion by disrupting the HIV env nanoclusters, highlighting the importance of the nanoclusters in the function of the viral glycoproteins[33]. More interestingly, the NiV-F distribution becomes more dispersed, characterized by smaller and less dense clusters, upon the mutation of two key residues, L53 and V108, at the hexameric interface, suggesting that the NiV-F clusters are likely to be the hexamer-of-trimer assemblies on the cell and viral membranes (**Fig. 3** and **4**).

The hexamer-of-trimer NiV-F is observed on the VLP surface by electron tomography[10]. The NiV-F hexamer-of-trimers are arranged into a soccer ball-like structure, with one trimer being part of multiple hexamer-of-trimers. Nonetheless, the hexagonal lattice has been reported for heamagglutinin-esterase-fusion (HEF) proteins on the surface of the influenza C virus[34] and Env glycoprotein on the Foamy virus[35]. The sharing of one trimer among hexamer-of-trimers and conformational arrangements in the ectodomain of viral glycoproteins were shown to stabilize the contacts for lattice formation[10,34,35]. In our study, the NiV-F clusters observed on the cell plasma membrane are more likely to be individual hexamer-of-trimers estimated by size (**Fig. 1**). We speculate that the formation of the hexagonal lattice may be a result of increased concentration of NiV-F on VLP membrane. A study on Measles virus shows only limited high order of MeV-F assemblies at some virus assembly sites in recMeV-(H-118 ∇41×) cells[36], however, we have not observed increased NiV-F localizations at NiV-M positive membrane domains on the cell body of NiV-M, F, and G co-expression PK13 cells[8]. Therefore, the formation of NiV-F lattice on the VLP membrane may occur either at a late stage of virus assembly or after budding. Additionally, cellular factors may also play a role in maintaining individual NiV-F hexamer-of-trimers on the plasma membrane, as a proteomic analysis reveals that NiV-F is an interacting partner of many vesicular trafficking and actin cytoskeleton factors[26,28].

We also identified that the endosomal components as key host factors in maintaining the NiV-F nano-organization on the cell membrane. Our data suggest that both the disruption of the F/AP-2 interaction and the inhibition of clathrin assembly by pitstop2 result in dispersed NiV-F distribution. AP-2 is the key adaptor of clathrin-mediated endocytosis. It binds cargo and PtdIns(4,5)P_2-containing membrane via multiple interface, and undergoes conformational changes to append to the clathrin lattice[25,37]. Our data indicate that AP-2-NiV-F interaction can enrich and strengthen the F nanoclusters (**Fig. 6A-F** and Fig. S7H), and potentially facilitate the uptake of NiV-F by endocytosis for endosomal cleavage and activation. It is reported that the clustering of CD44, modulated by *N*-glycosylations, facilitates the uptake of CD44 by endocytosis. Furthermore, the assembly of the clathrin coat at the plasma membrane may also strengthen the F clusters,

because pitstop2 that inhibits the clathrin-coat assembly by blocking the clathrin terminal domain[25] prevents the cluster formation of NiV-F. It is plausible that both clathrin and AP-2 facilitate NiV-F clustering on cell and virus membranes because of the similar organization of F on virus and cell membranes and the presence of clathrin and AP-2 in VLPs[26,28].

In conclusion, our observations provide direct evidence on the nano-organization and distribution of NiV-F on the cell and viral membranes and shed lights to the fusion activation mechanisms. Therefore, it would be critical to elucidate host factors that maintain NiV-F clusters and the interacting motif in NiV-F, which may represent a new therapeutic strategy for NiV infections. It would also be interesting to analyze the reorganization of the NiV-F clusters upon triggering by the NiV-G/receptor complex on live cell membranes by combining single-molecule imaging and the supported lipid bilayer technologies[12]. Additionally, a precise stoichiometry of individual NiV-F clusters on the cell and virus membranes could facilitate the vaccine design.

Materials and methods

Reagent type	Designation	Source or reference	Identifiers	Additional information
Cell line	HEK293T	ATCC	CRL-3216	
Cell line	PK13	ATCC	CRL-6489	
Cell line	HeLa	ATCC	CCL-2	
Cell line	Vero	ATCC	CCL-81	
DNA plasmid	NiV-F-FLAG and mutants	This paper		The FLAG tag was inserted after residue 104 of the codon-optimized NiV-F (GenBank accession no. AY816748.1). The hexameric interface mutants (Fig. 3)[10], LI4A mutant (Fig. 5)[21], and YA mutant (Fig. 6)[6], were constructed as previously published.
DNA plasmid	NiV-F-HA	This paper		The HA tag was inserted after residue 104 of the codon-optimized NiV-F (GenBank accession no. AY816748.1).
DNA plasmid	NiV-G-HA	Liu et al. 2018[11]		
DNA plasmid	NiV-M-GFP	Liu et al. 2018, Wang et al. 2010 [11,38]		The GFP gene was fused to the N-terminus of NiV-M gene (GenBank accession no. EU480491.1)
DNA plasmid	AP2μ2-mCherry	Christien Merrifield	Addgene 27672	
DNA plasmid	Untagged NiV-F			Codon-optimized NiV-F (GenBank accession no. AY816748.1).
DNA plasmid	NiV-F-AU1			The AU1 tag was inserted at the C terminal of the codon-optimized NiV-F (GenBank

				accession no. AY816748.1).
DNA plasmid	NiV-M-β-lactamase	Wolf et al., 2009[16] Landowski et al., 2014[17]		The β-lactamase gene was fused to the N-terminus of NiV-M gene (GenBank accession no. EU480491.1)
Chemical compounds, drug	E64d	Sigma-Aldrich	E8640-250UG	20uM
Chemical compounds, drug	Pitstop2	Sigma-Aldrich	SML1169-5MG	30uM
Chemical compounds, drug	Tris	EMD Millipore	648311-1KG	50 mM for TN buffer
Chemical compounds, drug	NaCl	Sigma-Aldrich	S9888-1KG	10 mM for TN buffer
Chemical compounds, drug	Glucose oxidase	Sigma-Aldrich	G2133-50KU	0.5 mg/ml for imaging buffer
Chemical compounds, drug	Catalase	Sigma-Aldrich	C100	40 μg/ml for imaging buffer
Chemical compounds, drug	Mercapto ethylamine (MEA)	Sigma-Aldrich	30070-10G	50 mM for SMLM imaging buffer
Chemical compounds, drug	HEPES	Fisher Scientific	15-630-080	25 mM for fusion buffer
Chemical compounds, drug	Glutamine	Fisher Scientific	25-030-081	2 mM for fusion buffer
Chemical compounds, drug	$CaCl_2$	Sigma-Aldrich	C7902	1 mM for fusion buffer
Chemical compounds, drug	Probenecid	Sigma-Aldrich	P8761-25G	2.5 mM for fusion buffer
Chemical compounds, drug	Solution D	Fisher Scientific	K1156	1:20 for Entry kinetics loading solution
Antibody	Anti-FLAG mouse monoclonal	Sigma-Aldrich	F1804	IF, SMLM: 1:100, Flow: 1:200; WB: 1:500-1:5,000
Antibody	Anti-HA rabbit polyclonal antibody	Biolegend	902301	IF: 1:900 WB: 1:2,000

Antibody	Anti-GFP goat polyclonal antibody	Abcam	Ab5450	WB: 1:1000
Antibody	Anti-mCherry rabbit polyclonal antibody	Abcam	Ab167453	WB: 1:2000
Antibody	Anti-β-lactamase mouse monoclonal	Santa Cruz Biotechnology	Sc-66062	WB: 1:1000
Antibody	Anti-mouse donkey polyclonal antibody, Alexa Fluor® 647 conjugated	Invitrogen	A31571	IF and SMLM: 1:400
Antibody	Anti-rabbit donkey polyclonal antibody, Alexa Fluor® 488 conjugated	Invitrogen	A21206	IF: 1:400
Antibody	Anti-mouse donkey polyclonal antibody, Alexa Fluor® 488 conjugated	Invitrogen	A21202	Flow: 1:400
Antibody	Anti-goat donkey polyclonal antibody, HRP conjugated	Jackson Immunoresearch	705-035-147	WB: 1:5,000
Antibody	Anti-mouse goat polyclonal antibody, HRP conjugated	Biorad	1705047	WB: 1:5,000
Antibody	Anti-rabbit goat polyclonal antibody, HRP conjugated	Biorad	1706515	WB: 1:5,000
Commercial assays and kits	µMACS anti-DYKDDDDK starting kit	Miltenyi Biotec	130-101-636	
Commercial assays and kits	Renilla Luciferase Assay System	Promega	E2820	
Commercial assays and kits	LiveBLAzer™ FRET-B/G Loading Kit with CCF2-AM	Invitrogen	K1032	

Commercial assays and kits	QIAamp Viral RNA Kits for RNA Extraction	QIAGEN	52904	
Commercial assays and kits	SuperScript™ III First-Strand Synthesis System	Invitrogen	18080051	
software	SMLM image reconstruction	Liu et al. 2018[11]		MATLAB Codes are available upon request.
software	ClusDoc	Pageon et al. 2015[15]		Codes were modified to process the data generated in the custom-built SMLM microscope.
software	OPTICS [18]	This paper		C++ Codes are available upon request.
software	One-dimensional convolutional neural network (1D CNN)	This paper		PYTHON Codes are available upon request.
software	Prism Graphpad	Dotmatics		
software	Flowjo	BD		

Cell lines and plasmids

PK13, HeLa, Vero and HEK293T cells were cultured at 37°C and 5% CO_2 in DMEM (Sigma-Aldrich, D6429) complemented with 10% fetal bovine serum (Invitrogen, 12483-020). Cells were passaged using phosphate-buffered saline (PBS, Invitrogen, 10010-049) and 0.25% Trypsin-EDTA solution (Invitrogen, 25002-072). Cells were monitored routinely for mycoplasma contamination using a mycoplasma detection PCR kit (ABM, G238). A FLAG (NiV-F-FLAG) or HA (NiV-F-HA) tag was inserted after residue 104 of codon-optimized NiV-F in pcDNA3.1 vector. An AU1(NiV-F-AU1) tag was inserted at the C-terminal of codon-optimized NiV-F in pCAGGS vector. The untagged NiV-F does not contain any epitope tag. NiV-F-YA, L53D, V108D, Q393L, and LI4A were produced by site-directed mutagenesis using the NiV-F-FLAG in pcDNA3.1 vector as a template[6,10,21]. AP2μ2-mcherry plasmid is a gift from Christien Merrifield (Addgene # 27672). The HA-tagged NiV-G, GFP-tagged NiV-M, and β-lactamase-NiV-M were constructed previously[7,16,38].

Immunofluorescence for SMLM

For SMLM imaging on cells, 1×10^5 PK13 or HeLa cells were seeded on coverslips (Marienfeld #1.5H, 18 mm) coated with 2.5 μg fibronectin (Sigma-Aldrich, F4759-2 mg) in a 12-well plate, and transfected with 1 μg NiV-F variants using lipofectamine 3000 (Invitrogen, L3000015) on the following day. E64d was dissolved in methanol and pitstop2 in DMSO as recommended by the manufacturer. E64d was added to cells at 3 hrs post-transfection for a total treatment time of 15 hrs. Pitstop2 was added to cells at 10 hrs post-transfection for a total treatment time of 8 hrs. At 18 hrs post-transfection, cells were fixed with PBS containing 4% paraformaldehyde (PFA; Electron Microscopy Sciences; 50980487) and 0.2% glutaraldehyde (Sigma-Aldrich, G5882-50 ml) for 90 min at room temperature. Cells were treated with signal enhancer image-IT-Fx (Life Technologies, I36933) for 30 min at room temperature, and then blocked using BlockAid (Life Technologies, B10710) for 1 hr at room temperature. The FLAG-tagged NiV-F and mutants were detected by the anti-FLAG mouse monoclonal antibody (Sigma-Aldrich, F1804) and an Alexa Fluor® 647 conjugated donkey anti-mouse secondary antibody (Invitrogen, A31571). Cells were incubated with primary antibody overnight at 4°C, and then with the secondary antibody for 1 hr at room temperature. Each antibody incubation is followed by five PBS washes, 5 min each time. Cells were then fixed in PBS containing 4% PFA for 10 min at room temperature.

SMLM setup, imaging, and data analysis

SMLM setup. Imaging was performed on a custom-built SMLM. Briefly, the microscope was built upon an apochromatic TIRF oil-immersion objective lens (Nikon, 60x; numerical aperture 1.49). Four lasers were used for excitation: a 639 nm laser (MRL-FN-639, 500 mW) for exciting Alexa Fluor® 647, a 532 nm laser (MGL-III-532-300 mW) for exciting cy3B, a 488 nm laser (MBL-F-473-300 mW) for exciting GFP, and a 405 nm laser (MDL-III-405-100 mW) for reactivating Alexa Fluor 647 and cy3B. For SMLM imaging, the exciting and reactivating lasers were combined into a single path using dichroic mirrors and then expanded and collimated using a beam expander. The incident light beam was focused on the back focal plane of the objective lens. A translation stage allowed the beam to be shifted between the center and edge of the objective lens so that the incident light emerging from the objective lens reaches the sample at various angles. For SMLM imaging of NiV-F at the cell and virus membranes at the cell-coverslip contact, the incident angle of the illumination light was adjusted to near or greater than the critical angle of the water-glass interface to allow total internal reflection and ensure low background fluorescence for single fluorophore detection[39]. The emission fluorescence was separated using appropriate dichroic mirrors and filters (Semrock) and detected by electron-multiplying charge-coupled devices (EMCCD; Ixon, Andor). The full width at half maxima of the image of the point spread function was magnified in size to ~3 camera pixels (106 nm per pixel), ensuring the optimal fluorophore localization[39]. A feedback loop, composed of a tracking camera (Andor Zyla SCOMS camera) and a computer-controlled piezo stage (Thorlabs 3-Axis NanoMax 300), was employed to control the sample drift to <1 nm laterally and 2.5 nm axially[40].

Before SMLM imaging, fluorescence beads (Life technologies, F8799) were added to samples as fiducial markers for drift control. Samples were immersed in imaging buffer [TN buffer (50 mM Tris (pH 8.0) and 10 mM NaCl), 0.5 mg/ml glucose oxidase, 40 μg/ml catalase, 10% glucose, and 50 mM mercaptoethylamine (MEA)][14]. The expression level of the protein of interest in individual cells was determined by measuring the average emission fluorescence intensity of an area of 27×27 μm^2. To ensure sample stability during SMLM, a fiducial marker was continuously tracked by the tracking camera. A brief procedure for SMLM imaging is described as follows: 1) the sample was exposed to the imaging light beam [639 nm laser (1 kW/cm^2)] at a 90° incident angle to cause a subset of the fluorophores to switch to the fluorescent state; 2) the incident light angle was adjusted close to or at the critical angle at the water-glass interface to achieve total internal reflection; 3) a low density of activated fluorophores were recorded to avoid fluorophore overlap; 4) another subset of fluorophores was stochastically activated by exposure to the activation light (405 nm). This process was repeated until 40,000 images were acquired. Custom-written software in MATLAB (Mathworks) was used to identify activated fluorophores in each image, determine their precise locations by Gaussian fitting, and reconstruct SMLM images[39]. Briefly, each image was first convolved with a Gaussian kernel to remove noise and background, and thresholded to search for local maxima. Next, two fitting steps were applied to determine the peak center position, the amplitude, and the width.

Then, filtering and trail generation were combined to remove erroneous peaks and group multiple peaks originating from one activated fluorophore. Lastly, a list of fluorophore positions was reconstructed into a SMLM image. Clusters of NiV-F localizations on cell surface resolved by SMLM were identified and characterized using ClusDoC[15]. The min points and ε were set at 4 and 20, respectively.

VLP production and immunofluorescence

To produce NiV VLPs, HEK293T cells were transfected by NiV-F-FLAG or mutants, NiV-G-HA, and NiV-M-GFP at a 9:1:5 ratio by using polyethylenimine (PEI) at 1 mg/ml (Polysciences, 23966-100). At 48hrs posttransfection, the supernatant of the cell culture was collected and subjected to ultracentrifugation on a 20% sucrose cushion at 125, 392 rcf for 90 min. The VLP-containing pellets

were resuspended in 5% sucrose-NTE buffer. VLPs were bound to 2.5 μg fibronectin-coated 18 mm coverslips at 4°C overnight, followed by fixation using PBS containing 4% PFA and 0.2% glutaraldehyde. The protocols of immunofluorescence, SMLM setup, and SMLM imaging for cells were followed to stain and image NiV-F-FLAG and mutants on VLPs using SMLM. A widefield image of GFP was acquired and superimposed on the SMLM image of NiV-F. VLPs were identified as GFP-positive particles. The distribution of NiV-F localizations on VLPs was analyzed by using a custom-written OPTICS algorithm based on C++ and Point Cloud Library. Briefly, OPTICS segregates closely-situated data points into clusters from a 3D SMLM dataset[18]. OPTICS algorithm depends on two parameters: 1) ε describes the radius for searching neighbors, and the number of neighbors of point p is called *N*ε(*p*); 2) *minPts* is a user-defined parameter; Point p is a core point if it has more than *p* neighbors around it (including point *p* itself). The core-distance and reachability-distance are calculated for cluster segregation. The core-distance is the Euclidean distance of the *minptsth* closest points to point *p* (Equation (1)).

$$CoreDist_{\varepsilon,minPts}(p) = \begin{cases} UNDEFINED, if\ N_\varepsilon(p) < minPts, \\ minPts_{th}\ smallest\ distance\ in\ N_\varepsilon(p), otherwise \end{cases} \quad (1)$$

The reachability-distance of another Point *p* to Point *p* is either the Euclidean distance between point *p* and point *p* or the core-distance of *p*, whichever is bigger (Equation (2)).

$$ReachDist_{\varepsilon,minPts}(t,p) = \begin{cases} UNDEFINED, if\ N_\varepsilon(p) < minPts, \\ \max\left(CoreDist_{\varepsilon,minPts}(p), EudDist(p,t), otherwise \right. \end{cases} \quad (2)$$

The process begins by randomly selecting a point (point A). If the number of neighbors of point A is larger than the user-defined minPts (set at 10), the algorithm outputs point A without a reachability-distance value. Next, OPTICS obtains point A's nearest neighbor (point B) and outputs the B-A reachability-distance value. Point B is the new starting point. OPTICS recalculates the reachability-distance of all unprocessed neighbors of point B and selects the next point to process, as described above. This process repeats until all points in the dataset have been visited. The final output of OPTICS is a sequence of reachability-distances for each point.

The classification of the ordered sequence of reachability-distances was performed by using custom-written one-dimensional convolutional neural network (1D CNN) based on Python and Tensorflow. Briefly, CNN extracts features from OPTICS output dataset by using convolutional layers for subsequent classification of the space information hidden in the OPTICS datasets. The convolutional layers use a 1D sliding window to slide along the sequence data[41]. Each sliding window captures local information and passes it to the next layer. Multiple CNN layers work sequentially to build a high-dimensional representation of the dataset. A fully connected layer that transforms high-dimensional features into classification results is achieved by CNN convolution. We use t-SNE (t-distributed stochastic neighbor embedding) to reduce dimensionality on a trained neural network layer for visualization in **Fig 4C**[42].

SDS-PAGE, and western blot analysis and co-immunoprecipitation

For western blot analysis to confirm the expression of NiV-F-FLAG and mutants, HEK293T cells were seeded in 6-well plate and transfected with 2.5 μg pcDNA3.1 empty vector, NiV-F-FLAG, or mutants. At 28 or 48 hrs posttransfection, cells were lysed in RIPA buffer (Millipore-Sigma, 20-188) supplemented with protease inhibitor (Sigma-Aldrich, 11836170001) on ice for 30 min. The cell lysates were collected after centrifuge at 16,000 ×g for 20 min at 4°C. The cell lysates were supplemented with 1x SDS loading dye [60 mM Tris-HCl (pH=6.8); 2% SDS; 10% glycerol, 0.025% Brophenol blue] and 15 mM DTT (Thermo Scientific, R0861), and heated at 95°C for denature. The denatured cell lysates were loaded into 10% polyacrylamide gels for SDS-PAGE. Proteins were transferred to PVDF membrane, pore size 0.45 μm (Cytiva, GE10600021).

Membrane was blocked with 1% Bovine serum albumin (Sigma-Aldrich, A9647-50G) in PBS and incubated with anti-FLAG mouse monoclonal antibody (Sigma-Aldrich, F1804). An HRP-conjugated goat anti-mouse secondary antibody and the clarity Western ECL substrate (BioRad, 1705060) were used for protein detection. Images were acquired using Chemic Doc MP Imaging System (BioRad).

For co-immunoprecipitation experiments, HEK293T cells were transfected with the following combinations 1) 2.3 µg empty pcDNA 3.1 vector and 0.2 µg AP2µ2-mcherry, 2) 0.2 µg AP2µ2-mcherry and 2.3 µg NiV-F-FLAG, and 3) 0.2 µg AP2µ2-mcherry and 2.3 µg NiV-F-YA. At 48 hrs post-transfection, cells from 1 well of a 6-well plate were washed with PBS and lysed in 200 µl lysis buffer provided with the µMACS DYKDDDDK isolation kit, and supplemented with protease inhibitors. Cells were isolated on ice for 30 min. Cell debris was removed by centrifuge at 16,000 x g for 20 min at 4°C. 60 µl of cell lysate was set aside for immunoblot analysis, and the rest was used for immunoprecipitation, as recommended by the manufacturer. 6 µl anti-DYKDDDDK microbeads (Miltenyi Biotec, 130-101-591) were added to 140 µl cell lysates and incubated for 30min on ice. µ columns (Miltenyi Biotec, 130-101-591) were prepared according to the manufacturer's instructions. Lysate ran over the columns, and microbeads were washed according to the manufacturer's instruction. 20 µl preheated elution buffer (95°C) was added to the column before eluting the bound immunoprecipitated protein in 50 µl elution buffer. Elute was separated by 10% SDS-PAGE, and proteins were immunoblotted by mouse anti-FLAG and rabbit anti-mcherry primary antibodies. The HRP-conjugated goat anti-mouse and goat anti-rabbit secondary antibodies were used for protein detection.

Flow cytometry

HEK293T cells were seeded in 6-well plate and transfected with 2.5 µg pcDNA3.1 empty vector, NiV-F-FLAG, or mutants. Cells were collected in 1 mL phosphate-buffered saline (PBS) containing 10 mM EDTA after 28hrs post-transfection. The collected cells were incubated on ice for 1 h with primary antibody mouse anti-flag diluted in 1:200. Samples were washed twice in fluorescence-activated cell sorting (FACS) buffer (0.1% FBS with PBS). After washing, samples were incubated with fluorescent anti-mouse Alexa Fluor 647 antibody 1:400 on ice for 45 min. After being washed twice again, samples were read on a flow cytometer (Attune® NxT™ Acoustic Focusing Cytometer, Thermo Fisher) The results were analyzed through FlowJo. The mean fluorescent intensities (MFI) were normalized to the MFIs of the NiV F-WT.

Cell-cell fusion

HEK293T cells were seeded in the 12-well plate and transfected with 1µg total DNA of NiV-G and wt-F or mutant-F with a 3:1 ratio using Lipofectamine 3000. Cells were fixed with 4% PFA after 18 hrs post-transfection. Four or more nuclei within a common cytoplasm were considered syncytium. Syncytia were quantified by counting the number of nuclei in the syncytium per 10 × filed (5 fields are counted per group) under microscope TE2000U.

Viral entry kinetics assay

HEK293T cells were loaded with CCF2-AM in the loading buffer by using a CCF2-AM loading kit (Invitrogen) and incubated at room temperature for 90 min. Loaded cells were washed three times and resuspended in 60 µl of cold fusion buffer (25mM HEPES, 2mMGlutamine, 1mM CaCl2, 2.5mM probenecid in HBSS). 110 µl fusion buffer, 10 µl of VLPs, and 60 µl of loaded cells were added into a black, clear-bottom 96-well plate on ice. The VLPs were allowed to attach to target cells at 4°C for 1 hr. Viral entry was measured by a Tecan fluorometer preheated to 37°C. Fluorescence was recorded every 3 min for 4 h. A blue-to-green (B/G) fluorescence ratio was determined for each well at each time point. The background control B/G ratio of VLPs expressing only MG and MF was then subtracted from each sample ratio as indicated, and the B/G ratio was plotted against time.

VSV/NiV pseudovirus production, quantitative PCR (qPCR), and viral entry quantification

HEK293T cells in a 10 cm dish were transfected with NiV-F-Flag and NiV-G-HA. pCDNA3.1 vector was transfected as the negative control. At 18-20 hrs post-transfection, cells were infected by a recombinant VSV-ΔG-renilla luciferase virus in infection buffer (0.1% fetal bovine serum in PBS). After 48 hrs, the supernatant was collected and concentrated by ultra-centrifugation through a 20% sucrose cushion in NTE buffer at 125,000 × g at 4℃ for 90 min. The supernatant was removed and the pellet was re-suspended in the appropriate amount of 5% sucrose in NTE buffer. The expression levels of NiV-F and -G proteins in pseudoviruses were analyzed by Western blot, and the VSV genome copy number was quantified by qPCR. Briefly, the viral RNA of NiV/VSV pseudoviruses was extracted by using a Qiagen viral RNA extraction kit (QIAGEN, 52904), reverse transcribed to cDNA by the SuperScript III first-strand synthesis system (Invitrogen, 18080051). The VSV viral cDNA was quantified by using a qPCR Taqman probes (FAM-CGG TAT TTT TCC ATA ATT CAA GTA ATC TGC T-TAMRA) and the VSV-P plasmid was used as a standard to establish the standard curve. To quantify virus entry, Vero cells in a 96-well plate were infected using 10-fold serial virus dilutions. Infections were done for 2 h in infection buffer. After 24 hrs, the luciferase activity was measured using a Renilla luciferase assay kit (Promega E2810). The relative light units (RLUs) were plotted against the viral genome copy number per milliliter in GraphPad Prism.

Acknowledgements

We thank the multiscale imaging facility for instrument use. We thank Dr. Youssef Chebli at McGill University and Dr. David Scriven at the University of British Columbia for the support on laser scanning confocal microscopy and single-molecule imaging, respectively. **Funding.** This work is supported by funding from the Canadian Institutes of Health Research to Q.L. (183861) and the Coronavirus Variants Rapid Response Network to Q.L. (175622). **Author contribution:** Conceptualization: Q.W. and Q.L.; Image acquisition: Q.W.; Data analysis and code writing: Q.W., J.L., and Q.L.; Functional analysis: Q.W., Y.L., V.K., G.L.M., J.W.; Resources: Q.L., Supervision: Q.L.; Funding Acquisition: Q.L.. Writing: original draft: Q.W., J.L., and Q.L.; revision: all authors. Competing Interests: The authors declare that they have no competing interests. Code, reagents, and data availability: Custom-written codes are deposited in GitHub or available upon request. Reagents can be provided by the corresponding author on a completed material transfer agreement. Requests for the reagents and data should be submitted to qian.liu3@mcgill.ca. **Declare of interests.** The authors declare no competing interests.

References

1. Navaratnarajah C.K., Generous A.R., Yousaf I., Cattaneo R (2020) **Receptor-mediated cell entry of paramyxoviruses: Mechanisms, and consequences for tropism and pathogenesis** *Journal of Biological Chemistry* **295**:2771–2786 https://doi.org/10.1074/jbc.REV119.009961

2. Haas G.D., Lee B (2023) **Paramyxoviruses from bats: changes in receptor specificity and their role in host adaptation** *Current Opinion in Virology* **58** https://doi.org/10.1016/j.coviro.2022.101292

3. Aditi, Shariff M (2019) **Nipah virus infection: A review** *Epidemiology & Infection* **147** https://doi.org/10.1017/S0950268819000086

4. Thibault P.A., Watkinson R.E., Moreira-Soto A., Drexler J.F., Lee B (2017) **Zoonotic potential of emerging paramyxoviruses: knowns and unknowns** *Adv Virus Res* **98**:1–55 https://doi.org/10.1016/bs.aivir.2016.12.001

5. Diederich S., Sauerhering L., Weis M., Altmeppen H., Schaschke N., Reinheckel T., Erbar S., Maisner A (2012) **Activation of the Nipah Virus Fusion Protein in MDCK Cells Is Mediated by Cathepsin B within the Endosome-Recycling Compartment** *J Virol* **86**:3736–3745 https://doi.org/10.1128/JVI.06628-11

6. Diederich S., Moll M., Klenk H.-D., Maisner A (2005) **The Nipah Virus Fusion Protein Is Cleaved within the Endosomal Compartment *** *Journal of Biological Chemistry* **280**:29899–29903 https://doi.org/10.1074/jbc.M504598200

7. Negrete O.A., Levroney E.L., Aguilar H.C., Bertolotti-Ciarlet A., Nazarian R., Tajyar S., Lee B (2005) **EphrinB2 is the entry receptor for Nipah virus, an emergent deadly paramyxovirus** *Nature* **436**:401–405 https://doi.org/10.1038/nature03838

8. Liu Q., Bradel-Tretheway B., Monreal A.I., Saludes J.P., Lu X., Nicola A.V., Aguilar H.C (2014) **Nipah Virus Attachment Glycoprotein Stalk C-Terminal Region Links Receptor Binding to Fusion Triggering** *J Virol* **89**:1838–1850 https://doi.org/10.1128/JVI.02277-14

9. Liu Q., Stone J.A., Bradel-Tretheway B., Dabundo J., Montano J.A.B., Santos-Montanez J., Biering S.B., Nicola A.V., Iorio R.M., Lu X (2013) **Unraveling a three-step spatiotemporal mechanism of triggering of receptor-induced Nipah virus fusion and cell entry** *PLoS Pathog* **9**

10. Xu K. *et al.* (2015) **Crystal Structure of the Pre-fusion Nipah Virus Fusion Glycoprotein Reveals a Novel Hexamer-of-Trimers Assembly** *PLoS Pathog* **11** https://doi.org/10.1371/journal.ppat.1005322

11. Liu Q., Chen L., Aguilar H.C., Chou K.C (2018) **A stochastic assembly model for Nipah virus revealed by super-resolution microscopy** *Nature Communications* **9** https://doi.org/10.1038/s41467-018-05480-2

12. Wong J.J., Chen Z., Chung J.K., Groves J.T., Jardetzky T.S (2021) **EphrinB2 clustering by Nipah virus G is required to activate and trap F intermediates at supported lipid bilayer–cell interfaces** *Sci. Adv* **7** https://doi.org/10.1126/sciadv.abe1235

13. Coelho S., Baek J., Graus M.S., Halstead J.M., Nicovich P.R., Feher K., Gandhi H., Gooding J.J., Gaus K (2020) **Ultraprecise single-molecule localization microscopy enables in situ distance measurements in intact cells** *Science Advances* **6** https://doi.org/10.1126/sciadv.aay8271

14. Dempsey G.T., Vaughan J.C., Chen K.H., Bates M., Zhuang X (2011) **Evaluation of fluorophores for optimal performance in localization-based super-resolution imaging** *Nature Methods* **8**:1027–1036 https://doi.org/10.1038/nmeth.1768

15. Pageon S.V., Nicovich P.R., Mollazade M., Tabarin T., Gaus K (2016) **Clus-DoC: a combined cluster detection and colocalization analysis for single-molecule localization microscopy data** *Mol Biol Cell* **27**:3627–3636 https://doi.org/10.1091/mbc.E16-07-0478

16. Wolf M.C., Wang Y., Freiberg A.N., Aguilar H.C., Holbrook M.R., Lee B (2009) **A catalytically and genetically optimized beta-lactamase-matrix based assay for sensitive, specific, and higher throughput analysis of native henipavirus entry characteristics** *Virol J* **6** https://doi.org/10.1186/1743-422X-6-119

17. Landowski M., Dabundo J., Liu Q., Nicola A.V., Aguilar H.C (2014) **Nipah Virion Entry Kinetics, Composition, and Conformational Changes Determined by Enzymatic Virus-Like Particles and New Flow Virometry Tools** *J Virol* **88**:14197–14206 https://doi.org/10.1128/JVI.01632-14

18. Ankerst M., Breunig M.M., Kriegel H.-P., Sander J (1999) **OPTICS: ordering points to identify the clustering structure** *SIGMOD Rec* **28**:49–60 https://doi.org/10.1145/304181.304187

19. Kiranyaz S., Avci O., Abdeljaber O., Ince T., Gabbouj M., Inman D.J (2021) **1D convolutional neural networks and applications: A survey** *Mechanical Systems and Signal Processing* **151** https://doi.org/10.1016/j.ymssp.2020.107398

20. Barrett C.T., Dutch R.E (2020) **Viral Membrane Fusion and the Transmembrane Domain** *Viruses* **12** https://doi.org/10.3390/v12070693

21. Webb S., Nagy T., Moseley H., Fried M., Dutch R (2017) **Hendra virus fusion protein transmembrane domain contributes to pre-fusion protein stability** *Journal of Biological Chemistry* **292**:5685–5694 https://doi.org/10.1074/jbc.M117.777235

22. Bonifacino J.S., Neefjes J (2017) **Moving and positioning the endolysosomal system** *Curr Opin Cell Biol* **47**:1–8 https://doi.org/10.1016/j.ceb.2017.01.008

23. Bonifacino J.S., Traub L.M (2003) **Signals for sorting of transmembrane proteins to endosomes and lysosomes** *Annu Rev Biochem* **72**:395–447 https://doi.org/10.1146/annurev.biochem.72.121801.161800

24. Mattera R., Farías G.G., Mardones G.A., Bonifacino J.S (2014) **Co-assembly of Viral Envelope Glycoproteins Regulates Their Polarized Sorting in Neurons** *PLOS Pathogens* **10** https://doi.org/10.1371/journal.ppat.1004107

25. von Kleist L. *et al.* (2011) **Role of the Clathrin Terminal Domain in Regulating Coated Pit Dynamics Revealed by Small Molecule Inhibition** *Cell* **146**:471–484 https://doi.org/10.1016/j.cell.2011.06.025

26. Johnston G.P. *et al.* (2019) **Nipah Virus-Like Particle Egress Is Modulated by Cytoskeletal and Vesicular Trafficking Pathways: a Validated Particle Proteomics Analysis** *mSystems* **4** https://doi.org/10.1128/msystems.00194-19

27. Pentecost M. *et al.* (2015) **Evidence for ubiquitin-regulated nuclear and subnuclear trafficking among Paramyxovirinae matrix proteins** *PLoS Pathog* **11** https://doi.org/10.1371/journal.ppat.1004739

28. Vera-Velasco N.M., García-Murria M.J., Sánchez Del Pino M.M., Mingarro I., Martinez-Gil L. (2018) **Proteomic composition of Nipah virus-like particles** *J Proteomics* **172**:190–200 https://doi.org/10.1016/j.jprot.2017.10.012

29. Chojnacki J., Eggeling C (2018) **Super-resolution fluorescence microscopy studies of human immunodeficiency virus** *Retrovirology* **15** https://doi.org/10.1186/s12977-018-0424-3

30. Muranyi W., Malkusch S., Müller B., Heilemann M., Kräusslich H.-G (2013) **Super-Resolution Microscopy Reveals Specific Recruitment of HIV-1 Envelope Proteins to Viral Assembly Sites Dependent on the Envelope C-Terminal Tail** *PLOS Pathogens* **9** https://doi.org/10.1371/journal.ppat.1003198

31. Laine R.F., Goodfellow G., Young L.J., Travers J., Carroll D., Dibben O., Bright H., Kaminski C.F (2018) **Structured illumination microscopy combined with machine learning enables the high throughput analysis and classification of virus structure** *eLife* **7** https://doi.org/10.7554/eLife.40183

32. McMahon A., Andrews R., Groves D., Ghani S.V., Cordes T., Kapanidis A.N., Robb N.C (2023) **High-throughput super-resolution analysis of influenza virus pleomorphism reveals insights into viral spatial organization** *PLOS Pathogens* **19** https://doi.org/10.1371/journal.ppat.1011484

33. Chen Y.-C., Sood C., Marin M., Aaron J., Gratton E., Salaita K., Melikyan G.B (2020) **Super-Resolution Fluorescence Imaging Reveals That Serine Incorporator Protein 5 Inhibits Human Immunodeficiency Virus Fusion by Disrupting Envelope Glycoprotein Clusters** *ACS Nano* **14**:10929–10943 https://doi.org/10.1021/acsnano.0c02699

34. Halldorsson S., Sader K., Turner J., Calder L.J., Rosenthal P.B (2021) **In situ structure and organization of the influenza C virus surface glycoprotein** *Nat Commun* **12** https://doi.org/10.1038/s41467-021-21818-9

35. Effantin G., Estrozi L.F., Aschman N., Renesto P., Stanke N., Lindemann D., Schoehn G., Weissenhorn W (2016) **Cryo-electron Microscopy Structure of the Native Prototype Foamy Virus Glycoprotein and Virus Architecture** *PLoS Pathog* **12** https://doi.org/10.1371/journal.ppat.1005721

36. Ke Z., Strauss J.D., Hampton C.M., Brindley M.A., Dillard R.S., Leon F., Lamb K.M., Plemper R.K., Wright E.R (2018) **Promotion of virus assembly and organization by the measles virus matrix protein** *Nat Commun* **9** https://doi.org/10.1038/s41467-018-04058-2

37. Kovtun O., Dickson V.K., Kelly B.T., Owen D.J., Briggs J.A.G (2020) **Architecture of the AP2/clathrin coat on the membranes of clathrin-coated vesicles** *Sci Adv* **6** https://doi.org/10.1126/sciadv.aba8381

38. Wang Y.E., Park A., Lake M., Pentecost M., Torres B., Yun T.E., Wolf M.C., Holbrook M.R., Freiberg A.N., Lee B (2010) **Ubiquitin-Regulated Nuclear-Cytoplasmic Trafficking of the Nipah Virus Matrix Protein Is Important for Viral Budding** *PLOS Pathogens* **6** https://doi.org/10.1371/journal.ppat.1001186

39. Bates M., Jones S.A., Zhuang X (2013) **Stochastic Optical Reconstruction Microscopy (STORM): A Method for Superresolution Fluorescence Imaging** *Cold Spring Harb Protoc* **2013** https://doi.org/10.1101/pdb.top075143

40. Tafteh R., Scriven D.R.L., Moore E.D.W., Chou K.C (2016) **Single molecule localization deep within thick cells; a novel super-resolution microscope** *J Biophotonics* **9**:155–160 https://doi.org/10.1002/jbio.201500140

41. Yu Y., Zhu Y., Li S., Wan D (2014) **Time Series Outlier Detection Based on Sliding Window Prediction** *Mathematical Problems in Engineering* **2014** https://doi.org/10.1155/2014/879736

42. Kobak D, Berens P (2019) **The art of using t-SNE for single-cell transcriptomics** *Nature Communications* **10** https://doi.org/10.1038/s41467-019-13056-x

Author information

Qian Wang
Institute of Parasitology, Faculty of Agricultural and Environmental Sciences, McGill University, Quebec, Canada

Jinxin Liu
Institute of Parasitology, Faculty of Agricultural and Environmental Sciences, McGill University, Quebec, Canada

Yuhang Luo
Institute of Parasitology, Faculty of Agricultural and Environmental Sciences, McGill University, Quebec, Canada

Vicky Kliemke
Institute of Parasitology, Faculty of Agricultural and Environmental Sciences, McGill University, Quebec, Canada

Giuliana Leonarda Matta
Institute of Parasitology, Faculty of Agricultural and Environmental Sciences, McGill University, Quebec, Canada

Jingjing Wang
Institute of Parasitology, Faculty of Agricultural and Environmental Sciences, McGill University, Quebec, Canada

Qian Liu
Institute of Parasitology, Faculty of Agricultural and Environmental Sciences, McGill University, Quebec, Canada, McGill Center for Viral Diseases, Lady Davis Institute, Montreal, Canada

For correspondence: qian.liu3@mcgill.ca

Editors

Reviewing Editor
Melike Lakadamyali
University of Pennsylvania, Philadelphia, United States of America

Senior Editor
Felix Campelo
Institute of Photonic Sciences, Barcelona, Spain

Reviewer #1 (Public review):

Summary:

In this work by Wang et al., the authors use single-molecule super-resolution microscopy together with biochemical assays to quantify the organization of Nipah virus fusion protein F (NiV-F) on cell and viral membranes. They find that these proteins form nanoscale clusters which favors membrane fusion activation, and that the physical parameters of these clusters are unaffected by protein expression level and endosomal cleavage. Furthermore, they find that the cluster organization is affected by mutations in the trimer interface on the NiV-F ectodomain and the putative oligomerization motif on the transmembrane domain, and that the clusters are stabilized by interactions among NiV-F, the AP2-complex, and the clathrin coat assembly. This work improves our understanding of the NiV fusion machinery, which may also have implications for our understanding of the function of other viruses.

Strengths:

The conclusions of this paper are well-supported by the presented data. This study sheds light on the activation mechanisms underlying the NiV fusion machinery.

https://doi.org/10.7554/eLife.97017.2.sa3

Reviewer #2 (Public review):

Summary:

In this manuscript, Wang and co-workets employ single molecule light microscopy (SMLM) to detect Nipah virus Fusion protein (NiV-F) in the surface of cells. They corroborate that these glycoproteins form microclusters (previously seen and characterized together with the NiV-G and Nipah Matrix protein by Liu and co-workers (2018) also with super-resolution light microscopy). Also seen by Liu and coworkers the authors show that the level of expression of NiV-F does not alter the identity of these microclusters nor endosomal cleavage. Moreover, mutations and the transmembrane domain or the hexamer-of-trimer interface seem to have a mild effect on the size of the clusters that the authors quantified. Importantly, it has also been shown that these particles tend to cluster in Nipah VLPs.

Strengths:

The authors have tried to perform SMLM in single VLPs and have shown partially the importance of NiV-F clustering.

Comments on the revised version:

I am happy with the answers the authors have provided to my questions

https://doi.org/10.7554/eLife.97017.2.sa2

Reviewer #3 (Public review):

Summary:

The manuscript by Wang and colleagues describes single molecule localization microscopy to quantify the distribution and organization of Nipah virus F expressed on cells and on virus-like particles. Notably the crystal structure of F indicated hexameric assemblies of F trimers. The authors propose that F clustering favors membrane fusion.

Strengths:

The manuscript provides solid data on imaging of F clustering with the main findings of:
- F clusters are independent of expression levels
- Proteolytic cleavage does not affect F clustering
- Mutations that have been reported to affect the hexamer interface reduce clustering on cells and its distribution on VLPs
- F nanoclusters are stabilized by AP

Comments on the revised version:

The authors addressed most of my previous concerns.

https://doi.org/10.7554/eLife.97017.2.sa1

Author response:

The following is the authors' response to the original reviews.

> ***Public Reviews:***
>
> ***Reviewer #1 (Public Review):***
>
> *Summary:*
>
> *In this work by Wang et al., the authors use single-molecule super-resolution microscopy together with biochemical assays to quantify the organization of Nipah virus fusion protein F (NiV-F) on cell and viral membranes. They find that these proteins form nanoscale clusters which favors membrane fusion activation, and that the physical parameters of these clusters are unaffected by protein expression level and endosomal cleavage. Furthermore, they find that the cluster organization is affected by mutations in the trimer interface on the NiV-F ectodomain and the putative oligomerization motif on the transmembrane domain, and that the clusters are stabilized by interactions among NiV-F, the AP2-complex, and the clathrin coat assembly. This work improves our understanding of the NiV fusion machinery, which may have implications also for our understanding of the function of other viruses.*
>
> *Strengths:*
>
> *The conclusions of this paper are well-supported by the presented data. This study sheds light on the activation mechanisms underlying the NiV fusion machinery.*
>
> *Weaknesses:*

The authors provide limited details of the convolutional neural network they developed in this work. Even though custom-codes are made available, a description of the network and specifications of how it was used in this work would aid the readers in assessing its performance and applicability. The same holds for the custom-written OPTICS algorithm. Furthermore, limited details are provided for the imaging setup, oxygen scavenging buffer, and analysis for the single-molecule data, which limits reproducibility in other laboratories. The claim of 10 nm resolution is not backed up by data and seems low given the imaging conditions and fluorophores used. Fourier Ring Correlation analysis would have validated this claim. If the authors refer to localization precision rather than resolution, then this should be specified and appropriate data provided to support this claim.

We thank reviewer 1 for these suggestions. We described key steps in imaging setup, singlemolecule data reconstruction, the OPTICS algorithm in cluster identification, and 1D CNN in

classification of the OPTICS data in the Materials and Methods section. We also provided a recipe for the imaging buffer. We refer to 10 nm localization precision rather than resolution. The localization precision achieved by our SMLM system is shown in the Author response image 1.

Author response image 1.

The localization precision of the custom-built SMLM. Shows the distribution of localization error at the x (dX), y (dY), and z (dZ) direction in nanometer of blinks generated from Alexa Flour 647 labeled to NiV-F expressed on the plasma membrane of PK13 cells. The lateral precision is <10 nm and the axial precision is < 20 nm.

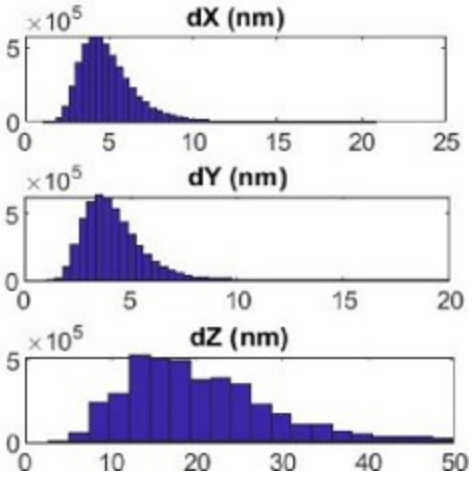

Reviewer #2 (Public Review):

Summary:

In this manuscript, Wang and co-workers employ single molecule light microscopy (SMLM) to detect NiV fusion protein (NiV-F) in the surface of cells. They corroborate that these glycoproteins form microclusters (previously seen and characterized together with the NiVG and Nipah Matrix protein by Liu and co-workers (2018) also with super-resolution light microscopy). Also seen by Liu and coworkers the authors show that the level of expression of NiV-F does not alter the identity of these microclusters nor

> *endosomal cleavage. Moreover, mutations and the transmembrane domain or the hexamer-of-trimer interface seem to have a mild effect on the size of the clusters that the authors quantified.*
>
> *Importantly, it has also been shown that these particles tend to cluster in Nipah VLPs.*

We thank reviewer #2 for the comments and suggestions. This paper is built on Liu et al 1 to further characterize the nanoclusters formed by NiV-F and their role in membrane fusion activation. While Liu et al. studied the NiV glycoprotein distribution at the NiV assembly sites to inform mechanisms in NiV assembly and release, Wang et al. analyzed the nanoorganization and distribution of NiV-F at the prefusion conformation, providing insights into the membrane fusion activation mechanisms.

> *Strengths:*
>
> *The authors have tried to perform SMLM in single VLPs and have shown partially the importance of NiV-F clustering.*
>
> *Weaknesses:*
>
> *The labelling strategy for the NiV-F is not sufficiently explained. The use of a FLAG tag in the extracellular domain should be validated and compared with the unlabelled WT NiV-F when expressed in functional pseudoviruses (for example HIV-1 based particles decorated with NiV-F). This experiment should also be carried out for both infection and fusion (including BlaM-Vpr as a readout for fusion). I would also suggest to run a time-of-addition BlaM experiment to understand how this particular labelling strategy affects single virion fusion as compared to the the WT.*

We thank reviewer #2 for this suggestion. We have made various efforts to validate the expression and function of FLAG-tagged NiV-F. The NiV-F-FLAG shows comparable cell surface expression levels and induces similar cell-cell fusion levels in 293T cells as that of untagged NiV-F 1. The NiV-F-FLAG also showed similar levels of virus entry as untagged NiV-F when both were pseudotyped on a recombinant Vesicular Stomatitis Virus (VSV) with the VSV glycoprotein replaced by a *Renilla* luciferase reporter gene (VSV-ΔG-rLuc; Fig. S1D). We also performed a virus entry kinetics assay using NiV VLPs expressing NiV-M-βlactamase (NiV-M-Bla), NiV-G-HA, and NiV-F-FLAG, NiV-F-AU1 or untagged NiV-F. The intracellular AU1 tag is located at the C-terminus of NiV-F (Genbank accession no. AY816748.1). However, we detected different levels of NiV-M-Bla in equal volume of VLPs, suggesting that the tags in NiV-F affect the budding of the VLPs (Author response image 2A). Therefore, we performed fusion kinetics assay by using VLPs expressing the same levels of NiV-M-Bla. Among them, the NiV-F-FLAG on VLPs shows the most efficient fusion between VLP and HEK293T cell membranes (Author response image 2B), significantly more efficient than that of untagged NiV-F and NiV-FAU1. However, we cannot attribute the enhanced fusion activity to the FLAG tag, because the readout of this assay relies on both the levels of β-lactamase (introduced by NiV-M-Bla in VLPs) and the NiV-F constructs. The tags in NiV-F could affect both the budding of VLPs and the stoichiometry of F and M in individual VLPs. We did not use the HIV-based pseudovirus system because the incorporation of NiV-F into HIV pseudoviruses requires a C-terminal deletion 2,3.

In summary, the FLAG tag does not affect cell-cell fusion 1 and virus entry when pseudotyped to the recombinant VSV-ΔG-rLuc viruses (Fig. S1D). Given that we do not observe any difference in clustering between an HA- and FLAG-tagged NiV-F constructs on PK13 cell surface (Fig. S1A-C), we conclude that the FLAG tag has minimal effect on both the fusion activity and the nanoscale distribution of NiV-F.

Author response image 2.

Viral entry is not affected by labeling of NiV-F. A) Western blot analysis of NiV-M-Bla in NiV-VLPs generated by HEK293T cells expressing NiV-M-Bla, NiV-G-HA and NiV-F-FLAG, untagged NiV-F, or NiV-F-AU1. Equal volume of VLPs were separated by a denaturing 10% SDS–PAGE and probed against β-lactamase (SANTA CRUZ, sc-66062). B) NiV-VLPs expressing NiV-M-BLa, NiV-G-HA, and NiV-F-FLAG, untagged NiV-F or NiV-F-AU1 expression plasmids were bond to the target HEK293T cells loaded with CCF2-AM dye at 4°C. The Blue/Green (B/G) ratio was measured at 37°C for 4 hrs at a 3-min interval. Results were normalized to the maximal B/G ratio of NiV-F-FLAG-NiV VLPs. Results from one representative experiment out of three independent experiments are shown.

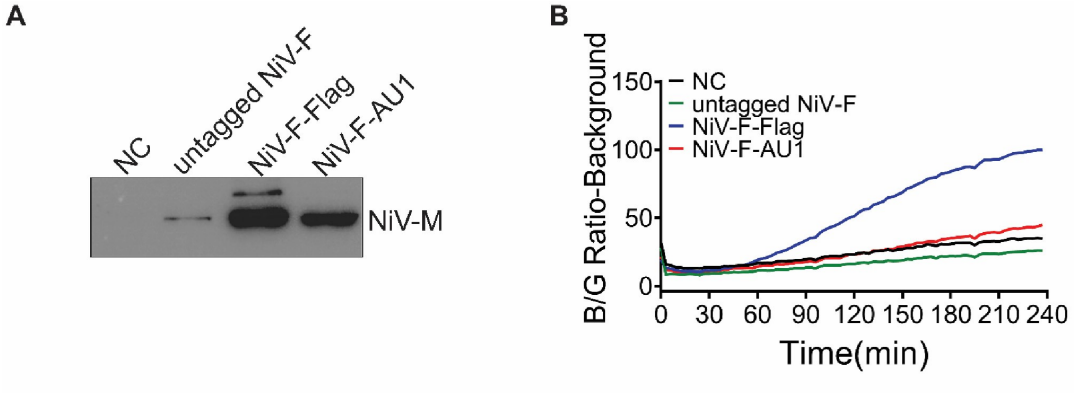

> *It would also be very important to compare the FLAG labelling approach with recent advances in the field (for instance incorporating noncanonical amino acids (ncAAs) into NiVF by amber stop-codon suppression, followed by click chemistry).*

We are greatly thankful for this comment from reviewer #2. Labeling noncanonical amino acids (ncAAs) with biorthogonal click chemistry is indeed a more precise labeling strategy compared to the traditional epitope labeling approach used in this paper. We will explore the applications of ncAAs labeling in single-molecule localization imaging and virus-host interactions in future projects.

In this paper, the FLAG tag inserted in NiV-F protein seems to have minimal effect on the NiV-F-induced virus entry and cell-cell fusion 1 (Fig. S1). Although the FLAG tag labeling approach may increase the detectable size of NiV-F nanoclusters due to the use of the antibody complex, it should not affect our conclusions drawn from the relative comparisons between wt and mutant NiV-F or control and drug-treated cells.

> *The correlation between the existence of microclusters of a particular size and their functionality is missing. Only cell-cell fusion assays are shown in supplementary figures and clearly, single virus entry and fusion cannot be compared with the biophysics of cell-cell fusion. Not only the environment is completely different, membrane curvature and the number of NiV-F drastically varies also. Therefore, specific fusion assays (either single virus tracking and/or time-of-addition BlaM kinetics with functional pseudoviruses) are needed to substantiate this claim.*

We thank Reviewer 2 for the suggestion. To support the link between F clustering and viruscell membrane fusion, we conducted pseudotyped virus entry and VLP fusion kinetics assays, as shown in revised Figure S4. The viral entry results (Fig. S4 E and F) corroborate that of the cell-cell fusion assay (Fig. S4A and B) and previously published data 4. The fusion

kinetics confirmed that the real-time fusion kinetics was affected by mutations at the hexameric interface, with the hypo-fusogenic mutants L53D and V108D exhibited reduced entry efficiency while the hyper-fusogenic mutant Q393L showed increased efficiency (Fig. S4G and H). The results were described in detail in the revised manuscript.

Additionally, we performed a pseudotyped virus entry assay on the LI4A (Fig. S6F and G) and YA (Fig. S7F and G) mutants to verify the function of these mutants on viruses in revised Supplemental Figures. Neither LI4A nor YA incorporated into the VSV/NiV pseudotyped viruses as shown by the Western blot analyses of the pseudovirions (Fig. S6F and S7F), and thus did not induce virus entry, consisting with the cell-cell fusion results (Fig. S6C, D and Fig. S7C, D). We did not perform the entry kinetic assay of these two mutants as they do not incorporate into VLPs or pseudovirions.

> *The authors also claim they could not characterize the number of NiV-F particles per cluster. Another technique such as number and brightness (Digman et al., 2008) could support current SMLM data and identify the number of single molecules per cluster. Also, this technology does not require complex microscopy apparatus. I suggest they perform either confocal fluorescence fluctuation spectroscopy or TIRF-based nandb to validate the clusters and identify how many molecule are present in these clusters.*

We thank reviewer 2 for this suggestion. Determining the true copy number of NiV-F in individual clusters could verify whether the F clusters on the plasma membrane are hexamer-of-trimer assemblies. Regardless, it does not affect our conclusion that the organization of NiV-F into nanoclusters affects the membrane fusion triggering ability. The confocal fluorescence fluctuation spectroscopy (FFS) and TIRF-based analyses are accessible tools for quantifying fluorophore copy numbers and/or stoichiometry based on fluorescence fluctuation or photobleaching. However, these methods are unable to quantify the number of proteins in individual clusters because they analyze fluorophores either in the entire cell (as in wide-field epifluorescence microscopy coupled with FFS and TIRF-coupled photobleaching) 5–7 or within a large excitation volume (confocal laser scanning microscopycoupled FFS) 8. Both of these volumes are significantly larger than a single NiV-F cluster, which has an average diameter of 24-26 nm (Fig. 1F).

The current SMLM setup is useful for characterizing the protein distribution and organization. However, quantifying the true protein copy number within a nanocluster is challenging because of the stochasticity of fluorophore blinking and the unknown labeling stoichiometry 9–11. To address the challenge in fluorophore blinking, quantitative DNA-PAINT (qDNA-PAINT) may be used because the on-off frequency of the fluorophores is tied to the well-defined kinetic constants of DNA binding and the influx rate of the imager strands, rather than the stochasticity of fluorophore blinking. Thus, the frequency of blinks can be translated to protein counting 12. To address the challenge in unknown labeling stoichiometry, DNA origami can be used as a calibration standard 11. DNA origami supports handles at a regular space with several to tens of nanometers apart, and the handles can be conjugated with a certain number of proteins of interest. The copy number of protein interest in the experimental group can be determined by comparing the SMLM localization distribution of the sample to that of the DNA origami calibration standard. Given the requirement of a more sophisticated SMLM setup and a high-precision calibration tool, we will explore the quantification of NiV-F copy numbers in nanoclusters in a future project.

> *Also, it is not clear how many cells the authors employ for their statistics (at least 30-50 cells should be employed and not consider the number of events blinking events. I hope the authors are not considering only a single cell to run their stats... The differences between the mutants and the NiV-F is minor even if their statistical analyses give a difference (they should average the number and size of the clusters per cell for a total of 30-50 cells with experiments performed at least in three different cells following the same*

> *protocol). Overall, it seems that the authors have only evaluated a very low number of cells.*

We disagree with this comment from Reviewer #2. The sample size for cluster analysis in SMLM images was chosen by considering the target of the study (cells and VLPs) and the data acquisition and analysis standards in the SMLM imaging field. We also noted the sample size (# of ROI and cells) in the figure legend.

Below, we compared the sample sizes in our study to those in similar studies that used comparable imaging and cluster analysis methods from 2015 to 2024. The classical clustering analysis methods are categorized into global clustering (*e.g.* nearest neighbor analysis, Ripley's K function, and pair correlation function) and complete clustering, such as density-based analysis (*e.g.* DBSCAN, Superstructure, FOCAL, ToMATo) and Tessellationbased analysis (*e.g.* Delaunay triangulation, Voronoii Tessellation). The global clustering analysis method provides spatial statistics for global protein clustering or organization (*e.g.* clustering extent), while the complete clustering approach extracts information from a single-cluster level, such as the morphology and localization density of individual clusters. We used the density-based analyses, DBSCAN and OPTICS, for cluster analysis on cell plasma membranes and VLP membranes.

Author response table 1.

The comparison of imaging methods, analysis methods, and sample size in the current study to other studies conducted from 2015 to 2024.

Study			Acquisition	Analysis	
Ref.	Year	Target		Methods	Sample size
Wang et al. (this study)	2024	NiV fusion protein in PK13, HeLa cells	dSTORM	DBSCAN, Hopkins	4-20 cells, ROI 40-242 per condition from 3 independent experiments.
Wang et al. (this study)	2024	NiV fusion protein in VLPs	dSTORM	OPTICS	40-200 VLPs from three independent experiments
Rubin-Delancy et al.[15]	2015	CD3 in T cells	PALM, dSTORM	Ripley, Bayesian	30 ROIs per condition.
Griffe et al.[14]	2017	LAT vesicles in T cells	iPALM	Ripley, Bayesian	5 cells per condition
Griffie et al.[15]	2018	CD4 in T cells	Live-cell PALM		6 cells
Caetano et al.[16]	2015	PACS, LAMP1 in HeLa cells	Ground State Depletion Microscopy	Densitybased, Ripley	5 cells per experiment (3 exp.)
Malkusch and Heilemann[17]	2016	HIV, gag, env in T cells	SMLM	DBSCAN, Ripley, OPTICS	1 cell
Zhang et al.[18]	2017	Salmonella typhimurium mutants in bacterial cells	FPALM	DBSCAN	58-60 bacterial cells.
Tobin et al.[19]	2018	HER2 receptor in breast cancer cells	dSTORM	Density pair correlation	17-23 cells
Levet et al.[20]	2015	Microtubules in Cos-7 cells, GluA1, tubulin, integrin-β3 in neuron cells	PALM, dSTORM	Voronoi	3 cells per condition
Peters et al.,[21]	2018	F-actin in T cells, microtubule network in HeLa cells	dSTORM	Voronoi, Ripley	3-5 cells
Levet et al.[22]	2019	Nuclear pore complex; microtubule, and actin cytoskeleton regulators	DNA-PAINT, dSTORM, and PALM	Voronoi	3-18 cells per condition.
Banerjee et al.[23]	2023	ULK in autophagy formation in HeLa cells	PALM	Spatial cross correlation	7-34 cells per condition
Pageon et al.[24]	2016	CD3ζ–PSCFP2 in Jurkat–OT-I cells	PALM	DBSCAN	4-6 cells
Cresens et al.[25]	2023	Flat clathrin laces in KM12L4a cell	PALM	DBSCAN	35 cells
Seeling et al.[26]	2023	Decn-1 in FγRIIb cell	dSTORM	DBSCAN	6-10 cells

> *They should also compare the level of expression (with the number of molecules per cell provided by number and brightness) with the total number of clusters.*

We thank reviewer 2 for this suggestion. We compared the level of expression with the total number of clusters for F-WT in Figure 1I in the main text.

> *The same applies to the VLP assay. I assume the authors have only taken VLPs expressing both NiV-M and NiV-F (and NiV-G). But even if this is not clearly stated I would urge the*

> *authors to show how many viruses were compared per condition (normally I would expect 300 particles per condition coming from three independent experiments. As a negative control to evaluate the cluster effect I would mix the different conditions. Clearly you have clusters with all conditions and the differences in clustering depending on each condition are minimal. Therefore you need to increase the n for all experiments.*

We thank reviewer 2 for this comment. We acquired and analyzed more images of NiV VLPs bearing F-WT, Q393L, L53D, and V108D. Results are shown in the revised Figure 4 and the number of VLPs (>300) used for analysis is specified in the figure legend. An increased number of VLP images does not affect the classification result in Figure 4C.

As for the suggestion on "evaluating the cluster effect at different mixed conditions", I assume that reviewer 2 would like to see how the presence of different viral structural proteins (F, M, and G) on VLPs could affect F clustering. We showed that the organization of NiV envelope proteins on the VLP membrane is similar in the presence or absence of NiV-M by direct visualization 27, suggesting that the effect of NiV-M on F-WT clustering on VLPs is minimal. We also show comparable incorporation of NiV-F among the NiV-F hexamer-oftrimer mutants (Fig. 4A). Therefore, we did not test the F clustering at different F, M, and G combinations in this paper. However, this could be an interesting question to pursue in a paper focusing on NiV VLP production.

> ***Reviewer #3 (Public Review):***
>
> *Summary:*
>
> *The manuscript by Wang and colleagues describes single molecule localization microscopy to quantify the distribution and organization of Nipah virus F expressed on cells and on virus-like particles. Notably the crystal structure of F indicated hexameric assemblies of F trimers. The authors propose that F clustering favors membrane fusion.*
>
> *Strengths:*
>
> *The manuscript provides solid data on imaging of F clustering with the main findings of:*
>
> *- F clusters are independent of expression levels*
>
> *- Proteolytic cleavage does not affect F clustering*
>
> *- Mutations that have been reported to affect the hexamer interface reduce clustering on cells and its distribution on VLPs - - F nanoclusters are stabilized by AP*
>
> *Weaknesses:*
>
> *The relationship between F clustering and fusion is per se interesting, but looking at F clusters on the plasma membrane does not exclude that F clustering occurs for budding. Many viral glycoproteins cluster at the plasma membrane to generate micro domains for budding.*
>
> *This does not exclude that these clusters include hexamer assemblies or clustering requires hexamer assemblies.*

We thank reviewer #3 for this question. We did not focus on the role of NiV-F clusters for budding in the current manuscript, although this is an interesting topic to pursue. In this manuscript, we observed that NiV VLP budding is decreased for some cluster-disrupting mutants, such as F-YA, and F-LI4A. however, F-V108D showed increased budding compared to F-WT (Fig. 4A). We also observed that VLPs and VSV/NiV pseudoviruses expressing L53D have little NiV-G (Fig. 4A, Fig. S4F and S4H), although the incorporation level of L53D is comparable

to that of wt F in both VLPs and pseudovirions (Fig. 4A and Fig. S4F). L53D is a hypofusogenic mutant with decreased clustering ability. Therefore, our current data do not show a clear link between F clustering and NiV VLP budding or glycoprotein incorporation.

We reported that both NiV-F and -M form clusters at the plasma membrane although NiV-F clusters are not enriched at the NiV-M positive membrane domains 1. This result indicates that NiV-M is the major driving force for assembly and budding, while NiV-F is passively incorporated into the assembly sites. The central role of NiV-M in budding is also supported by a recent study showing that NiV-M induces membrane curvature by binding to PI(4,5)P2 in the inner leaflet of the plasma membrane 28. However, the expression of NiV-F alone induces the production of vesicles bearing NiV-F 29 and NiV-F recruits vesicular trafficking and actin cytoskeleton factors to VLPs either alone or in combination with NiV-G and -M, indicating a potential autonomous role in budding 30. Additionally, several electron microscopy studies show that the paramyxovirus F forms 2D lattice interspersed above the M lattice, suggesting the participation of F in virus assembly and budding. Nonetheless, the evidence above suggests that NiV-F may play a role in budding, but our data cannot correlate NiV-F clustering to budding.

> *Assuming that the clusters are important for entry, hexameric clusters are not unique to Nipah virus F. Similar hexameric clusters have been described for the HEF on influenza virus C particles (Halldorsson et al 2021) and env organization on Foamy virus particles (Effantin et al 2016), both with specific interactions between trimers. What is the organization of F on Nipah virus particles? If F requires to be hexameric for entry, this should be easily imaged by EM on infectious or inactivated virus particles.*

We thank reviewer #3 for this suggestion. The hexamer-of-trimer NiV-F is observed on the VLP surface by electron tomography 4. The NiV-F hexamer-of-trimers are arranged into a soccer ball-like structure, with one trimer being part of multiple hexamer-of-trimers. The implication of NiV-F clusters in virus entry and the potential mechanism for NiV-F higherorder structure formation are discussed in the revised manuscripts.

> *AP stabilization of the F clusters is curious if the clusters are solely required for entry? Virus entry does not recruit the clathrin machinery. Is it possible that F clusters are endocytosed in the absence of budding?*

We thank reviewer #3 for this question. The evidence from the current study does not exclude the role of NiV-F clustering in virus budding. NiV-F is known to be endocytosed in the virus-producing cells for cleavage by Cathepsin B or L at endocytic compartments at a pH-dependent manner31–33 in the absence of budding. However, given that all cleaved and uncleaved NiV-F have an endocytosis signal sequence at the cytoplasmic tail and are able to interact with AP-2 for endosome assembly and the cleaved and uncleaved F may have similar clustering patterns (Fig. 2), we do not think NiV-F clustering is specifically regulated for the cleavage of NiV-F. A plausible hypothesis is that NiV-F clusters are stabilized by multiple intrinsic factors (e.g. trimer interface) and host factors (e.g. AP-2) on cell membrane for cell-cell fusion and virus budding. We linked the clustering to the fusion ability of NiV-F in this study, but the NiV-F clustering may also be important in facilitating virus budding. Once in the viruses, the higher-order assembly of the clusters (*e.g.* lattice) may form due to protein enrichment, and the cell factors may not be the major maintenance force.

> *Clusters are required for budding.*
>
> *Other points:*
>
> *Fig. 3: Some of the V108D and L53D clusters look similar in size than wt clusters. It seems that the interaction is important but not absolutely essential. Would a double mutant*

abrogate clustering completely?

We thank Reviewer #3 for the suggestion. We generated a double mutant of NIV-F with L53D and V108D (NiV-F-LV) and assessed its expression and processing. Although the mutant retained processing capability, it exhibited minimal surface expression, making it unfeasible to analyze its nano-organization on the cell or viral membrane.

Author response image 4.

The expression and fusion activity of Flag-tagged NiV-F and NiV-F L53D-V108D (LV). (A) Representative western blot analysis of NiV-F-WT, LV in the cell lysate of 293T cells. 293T cells were transfected by NiV-F-WT or the LV mutant. The empty vector was used as a negative control. The cell lysates were analyzed on SDS-PAGE followed by western blotting after 28hrs post-transfection. F0 and F2 were probed by the M2 monoclonal mouse antiFLAG antibody. GAPDH was probed by monoclonal mouse anti-GAPDH. (B) Representative images of 293T cell-cell fusion induced by NiV-G and NiV-F-WT or NiV-F-LV. 293T cells were co-transfected with plasmids coding for NiV-G and empty vector (NC) or NiV-F constructs. Cells were fixed at 18 hrs post-transfection. Arrows point to syncytia. Scale bar: 10um. (C) Relative cell-cell fusion levels in 293T cells in (B). Five fields per experiment were counted from three independent experiments. Data are presented as mean ± SEM. (D) The cell surface expression levels of NiV-F-WT, NiV-F-LV in 293T cells measured by flow cytometry. Mean fluorescence Intensity (MFI) values were calculated by FlowJo and normalized to that of F-WT. Data are presented as mean ± SEM of three independent experiments. Statistical significance was determined by the unpaired t-test with Welch's correction (*P<0.05, **P<0.01, ***P<0.001, ****P<0.0001). Values were compared to that of the NiV-F-WT.

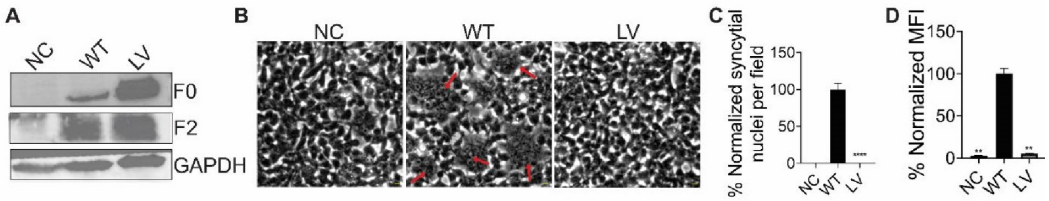

Fig. 4: The distribution of F on VLPs should be confirmed by cryoEM analyses. This would also confirm the symmetry of the clusters. The manuscript by Chernomordik et al. JBC 2004 showed that influenza HA outside the direct contact zone affects fusion, which could be further elaborated in the context of F clusters and the fusion mechanism.

We thank reviewer 3 for this suggestion. The distribution of F on VLPs was resolved by electron tomogram which showed that the NiV-F hexamer-of-trimers are arranged into a soccer ball-like structure 4. The role of influenza HA outside of the contact zone in fusion activation is an interesting phenomenon. It may address the energy transmission within and among clusters. We will pursue this topic in a future project.

Recommendations for the authors:

Reviewer #1 (Recommendations For The Authors):

• Please define all used abbreviations throughout the manuscript and in the SI.

We defined the abbreviations at their first usage.

• The sentence starting with "Additionally, ..." on line 155 appears to be incomplete.

We corrected this sentence.

> *• The statement starting with "As reported, ..." on line 181 should be supported by a reference.*

We added a reference.

> *• In Fig. 4C, it is unclear what the x and y axes represent.*

Fig. 4C is a t-SNE plot for visualizing high-dimensional data in a low-dimensional space. It maintains the local data structure but does not represent exact quantitative relationships. In other words, points that are close together in Fig. 4C are also close in the high-dimensional space, meaning the OPTICS plots, which reflect the clustering patterns, are similar for two points that are positioned near each other in Fig. 4C. Therefore, the x and y axes do not represent the original, quantitative data, and thus the axis titles are meaningless.

> *• The reference on line 306 appears to be unformatted.*

We reformatted the reference.

> ***Reviewer #2 (Recommendations For The Authors):***
>
> *The authors need to include the overall statistics for each experiment (at least 30 to 50 cells with three independent experiments are needed).*

We highlighted the sample size (number of ROI and number of cells) used for analysis in the figure legend. The determination of the sample size is justified in Table 1 in the response letter.

> *The authors need to generate a functional pseudovirus system (for example HIVpp/NiV F) to run both infectivity and fusion experiments (including Apr-BlaM assay).*

We tested viral entry using a VSV/NiV pseudovirus system and the viral entry kinetics using VLPs expressing NiV-M-β-lactamase. The results are presented in Fig. S1, S4, S6, and S7.

> ***Reviewer #3 (Recommendations For The Authors):***
>
> *Even low resolution EM data on VLPs or viruses would strengthen the conclusions.*

We thank this reviewer for the suggestion. We cited the NiV VLP images acquired by electron tomography 4, but we currently have limited resources to perform cryoEM on NiV VLPs.

References.

(1) Liu, Q., Chen, L., Aguilar, H. C. & Chou, K. C. A stochastic assembly model for Nipah virus revealed by super-resolution microscopy. *Nature Communications* 9, 3050 (2018).

(2) Khetawat, D. & Broder, C. C. A Functional Henipavirus Envelope Glycoprotein Pseudotyped Lentivirus Assay System. *Virology Journal* 7, 312 (2010).

(3) Palomares, K. *et al.* Nipah Virus Envelope-Pseudotyped Lentiviruses Efficiently Target ephrinB2Positive Stem Cell Populations In Vitro and Bypass the Liver Sink When Administered In Vivo. *J Virol* 87, 2094–2108 (2013).

(4) Xu, K. *et al.* Crystal Structure of the Pre-fusion Nipah Virus Fusion Glycoprotein Reveals a Novel Hexamer-of-Trimers Assembly. *PLoS Pathog* 11, e1005322 (2015).

(5) Bakker, E. & Swain, P. S. Estimating numbers of intracellular molecules through analysing fluctuations in photobleaching. *Sci Rep* 9, 15238 (2019).

(6) Nayak, C. R. & Rutenberg, A. D. Quantification of Fluorophore Copy Number from Intrinsic

Fluctuations during Fluorescence Photobleaching. *Biophys J* 101, 2284–2293 (2011).

(7) Salavessa, L. & Sauvonnet, N. Stoichiometry of ReceptorsReceptors at the Plasma MembranePlasma membrane During Their EndocytosisEndocytosis Using Total Internal Reflection Fluorescent (TIRF) MicroscopyMicroscopy Live Imaging and Single-Molecule Tracking. in *Exocytosis and Endocytosis: Methods and Protocols* (eds. Niedergang, F., Vitale, N. & Gasman, S.) 3–17 (Springer US, New York, NY, 2021). doi:10.1007/978-1-0716-1044-2_1.

(8) Slenders, E. *et al.* Confocal-based fluorescence fluctuation spectroscopy with a SPAD array detector. *Light Sci Appl* 10, 31 (2021).

(9) Annibale, P., Vanni, S., Scarselli, M., Rothlisberger, U. & Radenovic, A. Identification of clustering artifacts in photoactivated localization microscopy. *Nat Methods* 8, 527–528 (2011).

(10) Baumgart, F. *et al.* Varying label density allows artifact-free analysis of membrane-protein nanoclusters. *Nat Methods* 13, 661–664 (2016).

(11) Zanacchi, F. C. *et al.* A DNA origami platform for quantifying protein copy number in super-resolution. *Nat Methods* 14, 789–792 (2017).

(12) Jungmann, R. *et al.* Multiplexed 3D cellular super-resolution imaging with DNA-PAINT and Exchange-PAINT. *Nature Methods* 11, 313–318 (2014).

(13) Rubin-Delanchy, P. *et al.* Bayesian cluster identification in single-molecule localization microscopy data. *Nat Methods* 12, 1072–1076 (2015).

(14) Griffié, J. *et al.* 3D Bayesian cluster analysis of super-resolution data reveals LAT recruitment to the T cell synapse. *Sci Rep* 7, 4077 (2017).

(15) Dynamic Bayesian Cluster Analysis of Live-Cell Single Molecule Localization Microscopy Datasets - Griffié - 2018 - Small Methods - Wiley Online Library. https://onlinelibrary.wiley.com/doi/full/10.1002/smtd.201800008.

(16) Caetano, F. A. *et al.* MIiSR: Molecular Interactions in Super-Resolution Imaging Enables the Analysis of Protein Interactions, Dynamics and Formation of Multi-protein Structures. *PLOS Computational Biology* 11, e1004634 (2015).

(17) Malkusch, S. & Heilemann, M. Extracting quantitative information from single-molecule superresolution imaging data with LAMA – LocAlization Microscopy Analyzer. *Sci Rep* 6, 34486 (2016).

(18) Zhang, Y., Lara-Tejero, M., Bewersdorf, J. & Galán, J. E. Visualization and characterization of individual type III protein secretion machines in live bacteria. *Proceedings of the National Academy of Sciences* 114, 6098–6103 (2017).

(19) Tobin, S. J. *et al.* Single molecule localization microscopy coupled with touch preparation for the quantification of trastuzumab-bound HER2. *Sci Rep* 8, 15154 (2018).

(20) Levet, F. *et al.* SR-Tesseler: a method to segment and quantify localization-based super-resolution microscopy data. *Nature Methods* 12, 1065–1071 (2015).

(21) Peters, R., Griffié, J., Burn, G. L., Williamson, D. J. & Owen, D. M. Quantitative fibre analysis of singlemolecule localization microscopy data. *Sci Rep* 8, 10418 (2018).

(22) Levet, F. *et al.* A tessellation-based colocalization analysis approach for single-molecule localization microscopy. *Nat Commun* 10, (2019).

(23) Banerjee, C. *et al.* ULK1 forms distinct oligomeric states and nanoscopic structures during autophagy initiation. *Science Advances* 9, eadh4094 (2023).

(24) Pageon, S. V. *et al.* Functional role of T-cell receptor nanoclusters in signal initiation and antigen discrimination. *Proceedings of the National Academy of Sciences* 113, E5454–E5463 (2016).

(25) Cresens, C. *et al.* Flat clathrin lattices are linked to metastatic potential in colorectal cancer. *iScience* 26, 107327 (2023).

(26) Seeling, M. *et al.* Immunoglobulin G-dependent inhibition of inflammatory bone remodeling requires pattern recognition receptor Dectin-1. *Immunity* 56, 1046-1063.e7 (2023).

(27) Liu, Q. T. *et al.* The nanoscale organization of Nipah virus matrix protein revealed by super-resolution microscopy. *Biophysical Journal* 121, 2290–2296 (2022).

(28) Norris, M. J. *et al.* Measles and Nipah virus assembly: Specific lipid binding drives matrix polymerization. *Science Advances* 8, eabn1440 (2022).

(29) Patch, J. R. *et al.* The YPLGVG sequence of the Nipah virus matrix protein is required for budding. *Virol. J.* 5, 137 (2008).

(30) Johnston, G. P. *et al.* Nipah Virus-Like Particle Egress Is Modulated by Cytoskeletal and Vesicular Trafficking Pathways: a Validated Particle Proteomics Analysis. *mSystems* 4, e00194-19 (2019).

(31) Diederich, S. *et al.* Activation of the Nipah Virus Fusion Protein in MDCK Cells Is Mediated by Cathepsin B within the Endosome-Recycling Compartment. *J Virol* 86, 3736–3745 (2012).

(32) Diederich, S., Thiel, L. & Maisner, A. Role of endocytosis and cathepsin-mediated activation in Nipah virus entry. *Virology* 375, 391–400 (2008).

(33) Pager, C. T., Craft, W. W., Patch, J. & Dutch, R. E. A mature and fusogenic form of the Nipah virus fusion protein requires proteolytic processing by cathepsin L. *Virology* 346, 251–257 (2006).

https://doi.org/10.7554/eLife.97017.2.sa0